RELEASE FROM BIODEGRADABLE BIO-HYBRID HYDROGEL AND ELECTROSTIMULATION: TOWARD A BIOMIMETIC ENVIRONMENT FOR ENDOTHELIAL CELLS

A Dissertation

by

SARA ABASI

Submitted to the Office of Graduate and Professional Studies of
Texas A&M University
in partial fulfillment of the requirements for the degree of

DOCTOR OF PHILOSOPHY

Chair of Committee,	Anthony Guiseppi-Elie
Committee Members,	Melisa Grunlan
	Abhishek Jain
	Svetlana Sukhishvili
Head of Department,	Michael McShane

May 2020

Major Subject: Biomedical Engineering

ABSTRACT

A number of biochemical, mechanical, electrical and topographical factors serve as cues to orchestrate cellular responses. Tissue and regenerative engineering seek conditions wherein cells are exposed to cues similar in magnitude and temporal profile to those found in-vivo. For this purpose, a biomimetic, hybrid, degradable, hydrogel scaffold has been developed for use in a novel instrument that enabled electrostimulation of and paracrine release to cells in culture.

The hydrogel comprises HEMA and HPMA as synthetic components and methacrylated gelatin (GelMA) as natural, degradable component. Poly(HEMA-*co*-HPMA) hydrogels were studied for the influence of water content and distribution on key biotechnical properties. Poly(GelMA-*co*-HEMA-*co*-HPMA) were synthesized with pre-loaded FITC-dextran 40kDa as growth factor surrogate. The GelMA content was varied (0-87 mol%) to tune its collagenase degradation. Hydrogel formulation and factor payload, guided by the application requirements of compression modulus, degradation rate, release profile of factor, and the availability of motifs for cellular attachment, yielded scaffolds suitable for cell attachment, growth and proliferation.

An electrical cell stimulation and recording apparatus (ECSARA) equipped with in-situ electrical impedance spectroscopy (EIS) for real-time, non-invasive monitoring was developed to apply endogenous-range electric fields (EF) to cells in 3-D culture. The 24-well electroculture ware with trans-well Ti electrodes produced a uniform EF perpendicular to the plane of cells on porous, trans-well inserts. The system produced stable, reproducible, well-to-well temporal responses. The effect of EF on HUVECs was monitored with viability assay and EIS. Results indicated accelerated proliferation (alamarBlue assay) and early onset tight junction formation (EIS) in response to EF.

DEDICATION

To my parents, Fariba and Hamzeh, and my sisters and brothers for their unyielding support.

And to all my loved ones whom I wouldn’t be here without them.

ACKNOWLEDGEMENTS

I would like to thank my advisor and mentor, Professor Guiseppi-Elie, for welcoming me into his lab and his undeniable support of my growth not only as a scientist but as a human. I would also like to thank Professor Guiseppi-Elie for the support of this work as well as all previous work we have completed together over the years. I would like to thank my lab mates, Dr. John Aggas, Ankita Bhat, Brandon Walther, Lauren Whitney, and Naren Venkatesh for all the help and advice over the years we have worked together. I would also like to thank Dr. Aby Thyparambil, whose mentorship was extremely valuable as I started my research in C3B. I would like to thank Professor Ennio Tasciotti for his support and great feedback on my work. I would also like to thank all of the undergraduates whose hard work and dedication was essential to the completion of this body of work: Alycia Farida Sherback, Jasper Ocampo, Michael Zimmerman, Michael Florer, Iris Vallavanatt, and Ryan Davis. I would also like to thank Professor. Melisa Grunlan, Dr. Abhishek Jain, Dr. Corey Bishop, Dr. Jodie Lutkenhaus and Prof. Svetlana Sukhishvili for their time, feedback, and guidance toward this body of work.

CONTRIBUTORS AND FUNDING SOURCES

Contributors

This work was supervised by a dissertation committee consisting of Professor Anthony Guiseppi-Elie, Chair, Professor. Melisa Grunlan and Dr. Abhishek Jain of the Department of Biomedical Engineering and Professor Svetlana Sukhishvili of the Department of Materials Science and Engineering.

Funding Sources

Graduate study (September 2016 – May 2020) was supported by a Graduate Research Assistantship provided by Professor Anthony Guiseppi-Elie. Professor Anthony Guiseppi-Elie is founder and scientific director of ABTECH Scientific, Inc., manufacturer of microfabricated biochip substrates and devices used in this dissertation.

NOMENCLATURE

ϒ-APS	(3-aminopropyl)trimethoxysilan
τ	Time constant
ε	Void fraction
DI	Deionized water
DoH	Degree of hydration
DMPA	2,2-dimethoxy-2-phenylacetophenone
DSC	Differential scanning calorimetry
DAPI	4′,6-diamidino-2-phenylindole
EC	Endothelial cells
ECM	Extracellular matrix
ECSARA	Electrical Cell Stimulation and Recording Apparatus
EF	Electric field
FITC	Fluorescein isothiocyanate
FTIR	Fourier transform infrared spectroscopy
FRA	Frequency response analyzer
GelMA	Methacrylated gelatin
GUI	Graphical User Interface

HEMA	2-hydroxyethylmethacrylate
HEPES	4-(2-hydroxyethyl)-1-piperazineethanesulfonic acid
EIS	Electrical Impedance Spectroscopy
HMMA	N-[Tris(hydroxymethyl)methyl] acrylamide
HPMA	2-Hydroxypropyl methacrylate
HUVEC	Human umbilical vein endothall cells
I/O	Input/ Output
K_{cat}	Turnover number
K_M	Michaelis-Menten constant
LAP	Lithium phenyl-2,4,6-trimethylbenzoylphosphinate
M_{av}	Average molecular weight of monomers
M_c	molecular weight between cross-links
PBS	Phosphate-buffered Saline
PEGMA	Poly(ethylene glycol) monomethacrylate
PET	Polyethylene terephthalate
pNVP	Poly(N-vinylpyrrolidone)
Q_{DL}	Double layer phase constant element
Q_{OX}	Double layer capacitance of oxide layer

R_q	Root mean square surface roughness
RCBD	Randomized complete block design
R_{CT}	charge transfer resistance
R_M	Membrane resistance
R_S	Solution resistance
R_{OX}	Resistance of oxide layer
SEM	Scanning electron microscopy
TEER	Transepithelial/*transendothelial* electrical resistance
TEGDA	Tetra(ethylene glycol)diacrylate
T_g	Glass transition temperature
Ti	titanium
VE-cadherin	Vascular endothelial-cadherin
VEGF	Vascular endothelial growth factor
W_{ff}	Freezable free water
W_{nfb}	Non-freezable bound water
W_{fb}	Freezable bound water

TABLE OF CONTENTS

LIST OF FIGURES

LIST OF TABLES

1. INTRODUCTION

Advancements in healthcare science and engineering has opened a new frontier in the treatment of disease through tissue and regenerative engineering. Tissue engineering focuses on the *in-vitro* development of cell-laden constructs suitable for implantation to replace existing tissues and organs while regenerative engineering focuses on the design, fabrication, testing and validation of constructs to promote the body's native ability to regenerate. Clearly related, both are highly interdisciplinary with demands for integrative knowledge of organic and physical chemistry, surface science, biochemistry, biological chemistry, developmental biology, materials science and bioprocess engineering. All are dependent on our current understanding of molecular biology and cellular process. Such integrative knowledge has been applied in developing biomimetic conditions for our intervention to gain more favorable results *in-vivo*. Creating a biomimetic scaffold for cells is often the first step and there has been tremendous research in this area with and without specific pre-knowledge about the requirements for each specific cell, process condition and environment [1, 2].

Angiogenesis is a key element in tissue and regenerative engineering, organ-on-a-chip models, and in technologies where formation of a living, functional body of cells to tissues is sought. As prior studies have indicated, the efficient delivery of nutrients, molecular cues and removal of metabolic waste render the existence of blood vessels necessary in any naturally and laboratory-synthesized functional tissue/ organ [3]. Prerequisites of angiogenesis are endothelial cells and an appropriate environment for the cells to be driven toward tubular form, tubulogenic, and creation of a lumen. This underscores the importance of studying and understanding these cells, their interaction with scaffolds, responses to molecular cues, and responses to external electrical and

magnetic fields in detail. Endothelial cells used in research are mainly extracted as primary cells, however, Oswald et al. showed that they can be driven from differentiation of mesenchymal stem cells (MSCs) in the presence of VEGF [4]. The importance of the biochemical formulation of natural matrix is well known as shown in multiple studies. Lonza reported the vascular differentiation of MSCs when they were co-cultured with ECs. Different responses were observed in the presence of soluble VEGF, or ECM proteins such as fibronectin, laminin, and collagen [5]. Aizawa et al. developed an agarose-based 3-D scaffold with immobilized gradient of VEGF165, an isoform of VEGF-A, which had been shown to promote migration and proliferation of endothelial cells (ECs). They showed that ECs form tubular structures by penetrating a few hundreds of microns into the agarose in a VEGF165 dose-dependent fashion [6]. Such reports reveal the complexity of the process and possible synergistic effect of several factors to initiate specific responses. The provision of such factors must be considered for a successful simulation of *in-vivo* conditions.

Over the last century, scientists showed that cellular processes are not solely regulated by biochemical factors but, as inspired by nature, external factors and cues could be of similar importance. External cues range from topographical to mechanical, electrical, the effect of light etc. and refer to any stimuli that potentiates an *in-vivo* condition and has the potential to affect cellular behavior. The elastic modulus of the scaffold biomaterial, representation of stiffness, is well accepted as an influential factor in cellular behavior and response [7]. The scaffold modulus affects the growth but not the morphology of endothelial cells by changing the secretion of heparan sulfate proteoglycans (HSPGs), ECM proteins (collagen IV and fibronectin) and integrin expression (α_5, $\alpha_5\beta_1$, and $\alpha_v\beta_3$ subunits). A model has been suggested based on the cells' trying to accommodate the applied forces from the matrix stiffness by modifying their molecular biology

and secretome [8]. Differentiation of stem cells towards neuronal lineage are affected by substrate stiffness. Differentiation to neurons is supported by softer gels, while glial cells prefer stiffer substrates. The topography of the substrate has been shown to be significant in developmental processes [9]. The extracellular matrix (ECM), that fibrous network structure with macro/nano size features and signaling motifs allows and promotes cell interaction [10]. Aligned nanofibers provided topographical cues for endothelial cells which promoted spreading and proliferation while enabling control of their orientation [11, 12]. A less explored external cue is electrical signals. The two most critical functions of our body, nervous system and cardiac function, are via electrical signals leaving wonder for the rational of using electrical cues in tissue and regenerative engineering. Moreover, all developmental biology occurs in nascent electrical fields. Electrical signals and cues either in passive form, e.g. using conductive materials[13] or active, e.g. applying electrical stimulation, have been shown to affect cellular processes *in-vitro* and *in-vivo* [14]. Electrostimulation has been proven to positively support treatments and healing in several areas including pain control [15-17], wound healing [18, 19], regeneration [20, 21], and heart failure [22]; with all has been built upon the fundamental understanding of the effect of electrical signals on cells at the cellular and subcellular levels.

Engineered scaffolds can potentiate electric fields by their electrical properties, promote diffusive release of factors that serve as biochemical cues, provide topographical signaling by their surface morphology, deliver mechano-transduction cures via their modulus and promote attachment of recruited cells via biochemical signaling motifs. The prerequisite for providing all introduced factors is thus an exquisitely engineered scaffold. Hydrogels, a network polymer with high capacity for water absorption, have emerged as promising candidates for such exquisitely engineered scaffolds. Hydrogels could be synthesized from purely synthetic materials, such of

poly(ethylene glycol) (PEG), poly(2-Hydroxyethyl methacrylate) (pHEMA), polycaprolactone (PCL) , and poly(N-(2-Hydroxypropyl)methacrylamide) (pHPMA), or from natural biopolymers such as chitosan, alginate, fibrin, hyaluronic acid and gelatin, or from a co-polymer of both classes referred to as a biohybrid hydrogel. There exist other classifications such as electroconductive hydrogels which is based on a group of polymers with inherently conductive properties [23]. The temporal stability of hydrogels depends on their chemical formulation as well as the environment in which they function. As pointed out by the name, the environment is typically water-based which may affect the stability of some bonds via hydrolysis. As an example, the carbonyl group of ester is prone to hydrolysis therefore polymers containing ester bonds are subject to such hydrolytic degradation [24]. Although hydrolytically degradable hydrogels have been used effectively in biological studies [25-27], some application may require more control on the degradation process, e.g. in response to protease, rendering the hydrogel bioresponsive. Natural ECM proteins such as collagen, or peptides derived from them are appealing to synthesize hydrogels with cell-demand degradation. Such hydrogels provide an interactive platform for cells and allow remodeling per signaling requests from cells. Additionally, the degradation can be used to actuate the release of biomolecules which were preloaded into the hydrogel, e.g. growth factors to support cells [28, 29].

Synthetic hydrogels are cross-linked, three-dimensional polymeric networks synthesized from highly hydratable monomers and pre-polymers [30]. The resulting biotechnical polymer properties may be tuned by altering the monomer composition and/or cross-linker concentrations. Accordingly, hydrogels may be molecularly engineered for a wide range of biomedical applications, from transducer-active, stimuli-responsive polymers and actuators [31] to passive, bioreceptor hosting polymers in biosensors [32-34]. Using hydrogels as drug carriers in drug

delivery or as cell scaffolds in tissue and regenerative engineering are two emergent biomedical applications. Both these applications necessitate a detailed understanding of interactions of hosted biomolecules with the host polymer and their associated transport mechanism. Because of the importance of water in influencing both molecular interactions and transport, such an understanding begins with an appreciation of the various states of water and the distribution among these states within the hydrogel network. The degree of hydration (DoH) reflects the total amount of water imbibed by the hydrogel. Once imbibed, water within a hydrogel is described as comprising freezable free water, freezable bound water, and non-freezable bound water [35] and has been thoroughly reviewed. [36] For simplicity, the freezable free water and freezable bound water are generally grouped together as freezable water and is that portion that solvates the repeat units and occupies the interstices or nano-voids created by the expanded hydrogel [37]. This water freezes at the regular freezing temperature of water and is readily removed from the hydrogel. The non-freezable water is that portion which is strongly hydrogen-bonded and hence bound to the repeat units of the polymer network. The magnitude and extent of hydrogen bonding between water and the hydrogel's hydrophilic pendant groups influences the distribution amongst freezable, freezable bound and non-freezable bound water. [38] This consequently influences the extent of intra- and inter-chain hydrogen bonding within the polymer network. [39]

This thesis presents a simulating environment for endothelial cells touching on several requirements/ cues, 1) favorable stiffness 2) the need of a degradable scaffold that allows remodeling, 3) delivery of stimulating factors to cells to support/ guide their responses, and 4) delivery of endogenous-range electrical stimulation to cells. In the first chapter, a synthetic hydrogel based on HEMA and HPMA with varying cross-linker (TEGDA) concentrations and HEMA:HPMA ratio is introduced. A detailed analysis of these hydrogels for insight into their

analytical and physical characteristics is presented. The second chapter introduces a hybrid biodegradable hydrogel based on acryloyl-functionalized gelatin (GelMA) copolymerized with HEMA and HPMA. With detailed characterization and relevant mathematical models, it is shown how GelMA provides a mean toward a customized scaffold based on specific application requirements. The third chapter introduces a new bifunctional Electrical Cell Stimulation and Recording Apparatus (ECSARA) for applying electrical simultaneous to the cells that may be cultured on such scaffolds. The system provides a monitoring tool based on electrical impedance spectroscopy. The system requirements, its development, and detailed temporal and technical characterization with different physiological media are discussed. Finally, the application of the system in providing electric field to HUVECs is demonstrated. The last chapter summarizes the work and suggests several opportunities for further research based on the finding of the current work including integration of the degradable, cell-attracting scaffold in the presence of electric fields.

.

2. INFLUENCE OF WATER CONTENT AND DISTRIBUTION ON THE KEY BIOTECHNICAL PROPERTIES OF POLY(HEMA-*CO*-HPMA) HYDROGELS[1,2]

2.1.Introduction

Synthetic hydrogels are cross-linked, three-dimensional polymeric networks synthesized from highly hydratable monomers and pre-polymers [30]. A wide range of biologically relevant technical properties of synthetic hydrogels become critical when these polymers are to be considered for use in tissue and/or regenerative engineering [40-43]. The tunability of hydrogel properties has made hydrogels one of the most widely investigated classes of polymers in the biomedical field. Accordingly, hydrogels have evolved with wide and varied applications, from directly stimuli-responsive materials in sensors [31, 44] to bioreceptor hosting materials in biosensors [32-34]. Using hydrogel as drug carrier in drug delivery or as cell scaffold in tissue and regenerative engineering are two emergent biomedical applications. Both these applications necessitate a detailed understanding of interactions of hosted biomolecules with the host polymer and their associated transport mechanism. Because of the importance of water in influencing both molecular interactions and transport, such an understanding begins with an appreciation of the various states of water and the distribution among these states within the hydrogel network.

The degree of hydration of hydrogels (DoH = total water content / mass of hydrated hydrogel) is a measure of the total amount of water imbibed at equilibrium and is generally believed to control biotechnical properties. Once imbibed, water within a hydrogel may be described according to its

---

[1] Excerpted and reprinted with permission from "Biotechnical Properties of Poly(HEMA-co-HPMA) Hydrogels Are Governed by Distribution among Water States" by Abasi, Sara, Podstawczyk, D.A., Sherback, A.F., Guiseppi-Elie, A., 2019. ACS Biomaterials Science & Engineering, 5, 4994-5004, Copyright [2019] by © American Chemical Society. https://doi.org/10.1021/acsbiomaterials.9b00705

[2] Excerpted and repreinted with permission from "Distribution of water states within Poly(HEMA-co-HPMA)-based hydrogels" by Abasi, Sara, Podstawczyk, D.A., Davis, R., Guiseppi-Elie, A., 2019. Polymer, 185, 121978, Copyright [2019] by Elsevier. https://doi.org/10.1016/j.polymer.2019.121978

distribution among freezable free water (W_{ff}), freezable bound water (w_{fb}), and non-freezable bound water (W_{nfb}). The distribution of water among these states within hydrogels has been widely studied and recently reviewed [45]. The states of water and equilibrium water content have been studied via different techniques; mostly by differential scanning calorimetry (DSC), nuclear magnetic resonance (NMR) spectroscopy, and Fourier transform infrared spectroscopy (FTIR) [46, 47]. The non-freezable bound water (W_{nfb}) does not freeze within the temperature range probed by differential scanning calorimetry (DSC), remaining unfrozen even at temperatures lower than -100°C. The other two types of water freeze with freezable bound water melting at temperatures lower than freezable free water [45, 47]. A wide range of freezing temperatures of the freezable bound water has been reported, being closely influenced by chemical structure of the hydrogel, this temperature ranges from -40°C to very close to 0°C, the freezing temperature of free water [38, 48, 49]. Tamai et al. used the molecular dynamics simulations to explore the interaction of water and hydrogen bonded structures within hydrogels [50]. The results of their studies, and similar computational modeling, have given deeper insight into how the interactions of water with polymer and other water molecules govern the state of water within the hydrogel [51]. The freezable free water and freezable bound water are generally grouped together as freezable water (W_f) and is that portion that solvates the repeat units and occupies the interstices or nano-voids created by the expanded hydrogel [37]. The non-freezable bound water is the portion of water which is strongly hydrogen-bonded and hence bound to the repeat units of the polymer network and is first constituted as the hydrogel begins to swell, followed by freezable bound and finally freezable free water. Therefore, hydrogels possessing lower water content (less swellable) have relatively higher non-freezable water compared to highly swellable hydrogels of the same cross-linker concentration [46]. The extent and strength of interaction between water and the hydrogel's

hydrophilic main-chain and pendant groups and the pore size of the hydrogel which affect the capillary condensation of water in the hydrogels' pore [52], serve to influence the distribution amongst freezable free, freezable bound and non-freezable bound water [38]. The water within the hydrogel directly influences the characteristics of the hydrogel through the potentiation of inter- and intra-segmental hydrogen bonding that manifests as virtual crosslinks. Moreover, while freezable free water is readily available to fully solvate any hosted molecular inclusion and freezable bound water readily exchange between hydrogen bonding sites on the polymer and on the molecular inclusion, non-freezable bound water, because of its strong interaction with the host polymer, may not readily exchange between sites on the polymer and sites on the inclusion. Such characteristics influence diffusion, protein adsorption and consequently the biomaterial's interaction with living cells. [53-55]. Larger amounts of non-freezable bound water are expected to mitigate inter- and intra-segmental hydrogen bonding which would otherwise add to the effective cross-link density (virtual crosslinks) of the hydrogel.

Cross-linked poly(HEMA)-based hydrogels have been extensively studied for use in biomedical applications [56-59]. Copolymerization of HEMA with other monomers (vinyl, acrylates, methacrylates, etc.) have produced a wide range of stimuli-responsive hydrogels, including pH-responsive, [60] thermo-responsive [61], photo-chromic [62], and electroconductive hydrogels [63]. Poly(HEMA)-based hydrogels have been studied for the partitioning and release of biomolecules and ions [64] and for suitability to serve as tissue scaffolds [58] . With the aim of tailoring the key biotechnical properties and developing a softer material, HEMA was herein copolymerized with N-(2-hydroxypropyl) methacrylamide (HPMA). Since its introduction by Kopeček in 1973, poly(HPMA) has shown great promise for multiple biomedical applications [65] including drug conjugation and targeted drug delivery, tissue engineering scaffolds [66] and

controlled drug release [67, 68]. The introduction of the pendant amide serves to reduce both main and side chain mobility [69]. High molecular weight HPMA-based copolymers have been used in targeted drug delivery [70, 71] to enhance the mechanical characteristics and support function of natural polymers [72] and as a coating on implants to prevent biofouling.

The unique solvation properties of HEMA and HPMA monomers results in cross-linked polymer networks with different swelling kinetics, hydration characteristics, elastic modulus, and molecular mass transport properties. These properties are also well known to be influenced by extent of cross-linking and molecular composition. Understanding the complex interplay among these interacting factors is important for engineering control of properties for specific applications and for processing via different fabrication techniques. The cross-linking density of pure polymers grown via step-growth polymerization are readily rationalized by theory developed by Flory and Stockmayer based on statistical probability of monomers and multi-functional cross-linkers forming infinite networks. In the case of bi-functional cross-linkers, the cross-linking density (ρ) in the polymer comprising initial N_0 units is: $\rho = \nu/N_0$, where $\nu/2$ cross-links are introduced. [73] Accordingly, the molecular weight between cross-links M_c, may be calculated by deviding the average molecular weight of monomers (M_{av}) to the cross-linking density: $M_c = M_{av}/\rho$. [74] For free radical polymerization, such as the present case, the M_c (g/mol) can be experimentally measured with reference to the mechanical properties of the hydrogel according to: $M_c = RTc/G$ where R, T, and c are the molar gas constant (8.314 J/Kmol), absolute temperature (K), and polymer concentration (g/m^3) respectively, and G is the shear modulus of the hydrogel[75]. Understanding the complex interplay among these interacting factors is important for engineering control of properties for specific applications and for processing via different fabrication techniques. Tunability via cross-linker concentration and compositional variation is needed for

complex hydrogel formulations intended as bio-inks for microlithographic fabrication and 3-D printing [76]. This chapter reports on the synthesis, physicochemical and mechanical characterization of poly(HEMA-co-HPMA) hydrogels that were synthesized by UV cross-linking with the diacrylate monomer, TEGDA. Hydrogels were synthesized with different cross-linker concentrations (0.1, 0.5, 1.0 and 3.0 mol%) and with different HEMA to HPMA mole ratios corresponding to 1:0 (0% HPMA), 4:1 (20% HPMA), and 1:1 (50% HPMA). The characterization techniques were carefully selected to confirm suitability of this approach to tuning the biomedically relevant properties of poly(HEMA-co-HPMA) hydrogels. Moreover, the correlations between these individual components of the freezable water (W_f, W_{ff}, and W_{fb}) and the measured biotechnical properties of the hydrogels are discussed to introduce the water distribution as an indirect prosperity ruling other characteristics of hydrogels [77, 78].

2.2.Materials and Methods

2.2.1. Hydrogel formulation

Hydrogel cocktails of principally HEMA and HEMA-co-HPMA were formulated on a mol% basis as shown in **Table 1**. The mol% basis was used so every component is evaluated based on its functional groups. Moreover, the ratios of the monomers to the hydrogel volume remains constant as it is independent on the concentration of the monomers. The role of contributing monomers/ pre-polymers have been previously explored [79] and briefly mentioned in the table. Poly(HEMA)-based hydrogels were synthesized with cross-linker concentrations corresponding to 0.1, 0.5, 1.0 and 3.0 mol% TEGDA for investigation of the influence of cross-linker concentration. Similar hydrogels were synthesized wherein the ratio of HEMA to HPMA was set at 4:1 (20% HPMA, poly(HEMA-*co*-HPMA) (4:1)). Finally, similar hydrogels were synthesized with a fixed cross-linker concentration corresponding to 1.0 mol% TEGDA wherein the ratio of

HEMA to HPMA was set at 1:1 (50% HPMA, poly(HEMA-*co*-HPMA) (1:1)). Following formulation, cocktails were stirred and sonicated for extended time, purged with nitrogen gas, and pipetted into the wells (ϕ=4.5 mm and T=1.6 mm) of silicone isolators (JTR12R-2.0, Grace Biolabs, Bend, OR) that were supported on hydrophobic, OTS-silanized glass microscope slides.[76] The hydrogel discs were completely UV cross-linked for 5 min (CX-2000, UVP, Upland, CA), as DMPA resulted in fast reaction and high conversion, followed by unreacted monomer extraction and gradual hydration in ethanol:25 mM HEPES buffer (pH 7.4) mixtures (100/0, 75/25, 50/50, 25/75, and 0/100 v/v% sequentially) and stored in HEPES buffer at 4 ℃[76]. HEPES buffer was used because of its similarity to physiological osmolality, ionic strength and ion concentration found in blood plasma and interstitial fluid and is thus reflective of the environment where the hydrogel is primarily designed for use.

Table 1. Molecular components and mol% composition of the monomer cocktail components of the various hydrogels.

Component Mol% of TEGDA	Poly(HEMA)				Poly(HEMA-co-HPMA) (4:1)				Poly(HEMA-co-HPMA) (1:1)
	0.1	0.5	1.0	3.0	0.1	0.5	1.0	3.0	1.0
HPMA (high hydration)	0.0	0.0	0.0	0.0	17.4	17.4	17.3	16.9	43.3
HEMA (high hydration)	87.4	87	86.5	84.5	69.7	69.6	69.2	67.6	43.3
PEG(360)MA (n=6) (biocompatibility) [mol% is based on repeat unit]	5.0	5.0	5.0	5.0	5.0	5.0	5.0	5.0	5.0
HMMA (high hydration)	5.0	5.0	5.0	5.0	5.0	5.0	5.0	5.0	5.0
pNVP (adjust viscosity) [mol% is based on repeat unit]	2.0	2.0	2.0	2.0	2.0	2.0	2.0	2.0	2.0
DMPA (photoinitiator)	0.5	0.5	0.5	0.5	0.5	0.5	0.5	0.5	0.5
Ethylene Glycol/ Water (solvent)	20 wt%				20 wt%				20 wt%

The solubility parameter of HEMA and HPMA was calculated according to equation 1.

$$E_{coh} = \delta^2 V \quad (1)$$

Where E_{coh} (J mol^{-1}) is cohesion energy, V (cm^3 mol^{-1}) is the molar volume of the group being considered and δ ($J^{1/2}$ $cm^{-3/2}$) is the solubility parameter. The echo and V was calculated based on group contribution according to Federos [80].

The diffusion coefficient was calculated based on equation 2**.**

$$D_{AB} = \frac{8.2 \times 10^{-8}\ T}{\mu_B\ V_A^{1/3}} \left[1 + \left(\frac{3\ V_B}{V_A}\right)^{2/3}\right] \quad (2)$$

Where D_{AB} (cm^2 s^{-1}) is the diffusion coefficient of solute A in solvent B. T is temperature (K) here 296.15 K, μB is the solvent viscosity (mPa) here for water 0.889 mPa, V_A is the molar volume (cm^3 mol^{-1}) of liquid solute, and V_B is molar volume (cm^3 mol^{-1}) of the solvent at its normal boiling point here water (18 cm^3 mol^{-1}) [81]. Molar volume (V_A) of HEMA and HPMA was calculated based on the group contribution to be 116.7 and 117.8 cm^3 mol^{-1}, respectively.

2.2.2. Chemical and FTIR analysis

Attenuated total reflectance–Fourier transform infrared (ATR-FTIR) spectra were recorded on a Bruker Vertex 70 instrument equipped with ATR accessory within the scan range of 4000-400 cm^{-1} and a resolution of 1 cm^{-1}. The measurements were repeated nine times to produce reproducible spectra of the hydrogels.

2.2.3. Degree of hydration, water distribution and glass transition temperature

The degree of hydration (DoH) of the hydrogels was determined using gravimetric analysis as previously described with more details in Supporting Information. [82] Briefly, hydrogel discs were weighed following equilibrium hydration (M_{HG}) in HEPES buffer and then weighed again once they were completely dehydrated following lyophilization (M_{DG}). Dehydration was accomplished by freezing hydrogels at -80°C overnight followed by 48 h lyophilization under 0.01

mbar at -50°C using a FreeZone 2.5 (Labcono). The DoH was then calculated according to equation 3.

$$DoH\ (wt\%) = \left(\frac{M_{HG} - M_{DG}}{M_{HG}}\right) \times 100\% \quad (3)$$

Water distribution and glass transition temperature (T_g) were determined by thermal analysis using a DSC Q20 (TA Instruments, DE) on fully hydrated samples in Tzero Hermetic Aluminum Pans (DSC #84012 Premium pan/hermetic lid set) and run from -40 to 200 ℃ in the Heat-Cool-Heat cycle at a heating/cooling rate of 10°C/min. For determining water distribution, the calorimetric measurements were performed with a DSC Q20 (TA Instruments, DE) on fully hydrated samples in Tzero Hermetic Aluminum Pan in a Heat-Cool-Heat cycle from -40°C to 200°C at a rate of 10°C/min. The first heating cycle was used to calculate the freezable water content (W_f) comprising freezable bound (W_{fb}) and freezable free (W_{ff}) water according to equation 4.

$$\frac{W_f}{M_{HG}} = \frac{\Delta H_f}{\Delta H_0} \quad (4)$$

Where M_{HG} and M_{DG} are the mass of hydrogel at equilibrium and dried hydrogel, respectively, ΔH_0 is the standard enthalpy of water fusion (333.5 J/g at 0°C) and ΔH_f is the enthalpy of thermal transition or fusion of water at the melting point. The thermal transition was further deconvoluted by fitting to two Gaussian curves using OriginPro 2019. In this way the W_{fb} and W_{ff} portions of water were determined. The baseline was taken as a straight line connecting the beginning and ending of the endothermic transition. The enthalpy of fusion of water, normally 333.5 J/g at 0°C, was adjusted at temperatures below 0°C according to the experimental data reported by Higuchi and Iijima which was determined using a poly(vinyl alcohol-co-itaconic acid) hydrogel [46]. To calculate the W_{fb} and W_{ff}, the ratio $\Delta H_f/\Delta H_0$ in equation 2 was replaced with the enthalpy corresponding to the peak occurring at lower and higher temperatures, respectively. Knowing the

W_{fb} and W_{ff}, DoH and hydrogel mass, W_{nfb} was determined as the difference between total water content and freezable water content within the hydrogel.

The glass transition temperature was extracted from the second DSC heating cycle and calculated using Universal Analysis 2000 [58].

2.2.4. SEM and void fraction

The void fraction (ε) of hydrogel was determined by measuring the density of hydrogel when being hydrated in HEPES buffer according to equation 5.

$$\varepsilon = (\frac{M_{HG}-M_{DG}}{\rho_{HEPES}})/(\frac{M_{HG}}{\rho_{HG}}) \quad (5)$$

Where M_{HG} and M_{DG} stand for mass of hydrated and dry hydrogels, respectively; and ρ_{HG} and ρ_{HEPES} represent density of HEPES and fully hydrated hydrogel, respectively. More information on calculation of hydrogel density is available in Supplemental Information.

For SEM measurement, the hydrated hydrogels were frozen in liquid nitrogen tank in the cryovials for 8 h. The frozen specimens were freeze-fractured followed by drying in Turbo Vap V500 (Caliper LifeSciences, Hopkinton, MA) at 37°C for 48 h [83]. The hydrogels were then coated with 5 nm platinum nanoparticles (Sputter Coater 208 HR by Cressington, UK) and the SEM images were collected using SEM (JEOL JSM-7500F, JP) at X1000 magnification. The root mean square (R_q) representing the roughness of surfaces was measured using SurfCharJ plugin in ImageJ freeware [84].

The density of hydrogel was calculated by measuring the mass and volume of fully hydrated hydrogel in HEPES. The volume of hydrogel was measured with the fluid displacement technique. The fully dehydrated hydrogel was placed in a gradual cylinder with known volume of HEPES (V_1). The cylinder was covered to avoid evaporation, and the hydrogel was fully hydrated in the cylinder for 24 hours. After that, the hydrogel was removed, and the volume of HEPES after

hydrogel removal (V_2) was recorded. The volume of hydrogel calculated to be the difference of V_1 and V_2. Accordingly, hydrogel mass (W_{HG}) was measured using an analytical balance. The density of hydrogel (ρ_{HG}) calculated according to equation 6.

$$\rho_{HG} = \frac{V_1 - V_2}{W_{HG}} \quad (6)$$

2.2.5. Elastic modulus measurement

The elastic modulus of fully hydrated hydrogels was measured using an Instron 3345 (Norwood, MA) with a 1 kN pre-load cell. Using compression extension mode, the hydrogels were tested with a 0.1 N pre-load force over 5% strain. The elastic modulus was extracted from the linear part of the stress-strain curve.

2.2.6. Swelling kinetics by gravimetric technique

Fully hydrated hydrogel disks were dried in a TurboVap and rehydrated in HEPES buffer. At designated times, disks were taken out, excess buffer removed with Kimwipes and weighted with an analytical balance. The data were normalized between 0 and 1, corresponding to the mass of dried (M_0) and fully hydrated hydrogel at equilibrium (M_∞), respectively. The kinetics of swelling was interrogated using the characteristic time constant ($\boldsymbol{\tau}$, time required to absorb 63.2% of the total water content) of the device under test. The transport mechanism during swelling was studied using well-established transport models presented in the Supporting Information [85, 86]. MATLAB (2018b) was used for all curve fitting analysis and R^2 (square of sum of residuals) and SSE (summed square of residuals), which is the ratio of total deviation of the response values from the fit to the response values, were reported for the goodness of fit. An SSE value close to zero indicates the model best fits the data.

To study the transport mechanism during swelling, the swelling kinetics data was fitted to an empirical equation (equation 7) that describes the and transport mechanism [86, 87].

$$M_t/M_\infty = kt^n \quad (7)$$

where M_t/M_∞ is the fractional mass of hydrogel at time *t* to its equilibrium mass. This relation is valid only for the first 60% of the data.

2.2.7. Release of FITC labeled dextran

The release of fluorescently labeled dextran serves as a probe of the architecture of the hydrogel from an analysis of the dextran release rate from the hydrogel. Hydrogel cocktails and discs (V=150 mm^3) were formulated to contain 1 mg/mL FITC-labeled dextran (40 kDa) and placed in 2 mL of HEPES buffer upon cross-linking. Experiments were designed to provide an ideal sink for dextran release. At predetermined time points, 2 µL aliquots were removed from the gently shaking plate and transferred to a Take-3® (BioTek) plate. The fluorescence intensity was monitored using a plate reader (Synergy HT, BioTek) at Ex/Em 415/520 nm wavelengths over a 72-h period. The data were normalized between 0 and 1, corresponding to the mass of released dextran at time 0 (M_0) and equilibrium (M_∞), respectively. The early and late apparent diffusion coefficients extracted from the kinetics of released molecules was performed using well-established models [64, 88-90]. More detail is available in Supporting Information.

To study the transport mechanism of release, several mathematical models was applied. The early and late apparent diffusion coefficients were calculated according to equations 8 and 9 [91].

$$\frac{M_t}{M_\infty} = 4\left(\frac{D_E t}{\pi\delta^2}\right)^{0.5} \quad (8)$$

$$\frac{M_t}{M_\infty} = 1 - \frac{8}{\pi^2}\, exp\left(-\frac{\pi^2 D_L t}{\delta^2}\right) \quad (9)$$

where M_t and M_∞ is the amount of the solute released at time *t* and at equibrium respectively and where M_t/M_∞ is the fraction of released dextran, D_E and D_L are early and late apparent diffusion coefficients, respectively, and δ is the diffusional distance. The fluorescence intensity was related to the relative concentration of dextran using a calibration curve. The mechanism of release was inferred from data analyis according to well-established methods [64]. The data were normalized and analyzed similar to the gravimetry data in section 3.8. Additionally, data were described with **e**quation 10 [91].

$$M_t/M_\infty = k_1 t^{0.5} + k_2 t \quad (10)$$

where $k_1 t^{0.5}$ describes the Fickian release or diffusional-controlled release and $k_2 t$ describes the non-Fickian or relaxation-controlled release [86].

2.2.8. Statistical analysis

Student t-test was applied using JMP 14.2.0 (SAS Institute) and p-values of < 0.05 were considered significant and indicated with an asterisk symbol (*). All measurements were done in triplicate unless otherwise indicated. The Pearson product-moment correlations among the total hydration, the freezable water, the non-freezable bound water, and the freezable: non-freezable bound water ratio with the key biotechnical parameters of the various hydrogels were studied using the Multivariant method in JMP.

2.3. Results

2.3.1. Chemical analysis of hydrogel composition by FTIR

The hydrogel precursor cocktails used in this work were formulated for spin-coating and microlithographic fabrication as well as for extrusion 3-D printing [76]. The copolymerization of the principal monomers, HEMA and HPMA, being of similar molecular weight (MW = 130.14

and 143.18 g/mol, respectively), calculated diffusivity (D_{cal} = 8.91 x10^{-6} and 8.80 x10^{-6} cm^2/s, respectively), and chemical reactivity, was expected to yield a random copolymer network. Accordingly, the composition of the resulting copolymer was expected to reflect the starting composition of the reactants within the formulation. The ATR-FTIR spectra of poly(HEMA) and poly(HEMA-co-HPMA) (4:1) are shown in **Figure 1**. Although, the hydrogel cocktails are mixtures of few different precursors, the most intensive peaks correspond to the HEMA and HPMA since they are the dominant components of the hydrogels. However, due to the presence of other constituents in the hydrogel cocktail, the frequencies may be shifted to wavenumbers other than those characteristic for pure polymers. The peak at 1530 cm^{-1} in the poly(HEMA-co-HPMA) (4:1) spectrum is ascribed to the 2° amide bending vibration, thereby confirming that HPMA had been successfully incorporated into the hydrogel. The characteristic peak in the region of 3319 - 3362 cm^{-1}, normally at 3400 cm^{-1} in pure, bulk water where there is an average of two to three hydrogens bonds per molecule, was observed in both polymers and corresponds to the stretching vibration of hydrogen bonded O-H bands of the hydroxyl group [92]. The hydrogen bonds resulting from water-hydrogel interactions are strong and linear, thus they produce a broad, intensive peak, which overlaps stretching vibration of weaker O-H covalent bonds in a polymer matrix. The O-H stretching peak shifted to lower wavenumber (3350 cm^{-1}) in poly(HEMA-co-HPMA) (4:1) compared to poly(HEMA) (3362 cm^{-1}). The HPMA repeat unit has nitrogen in its pendant group which is more electronegative than oxygen, suggesting stronger hydrogen bonds in O-H….N compared to O-H….O; [93] that could account for the shift of the O-H stretching peak to lower wavenumbers which occurs when the strength of hydrogen bonds increases [94].

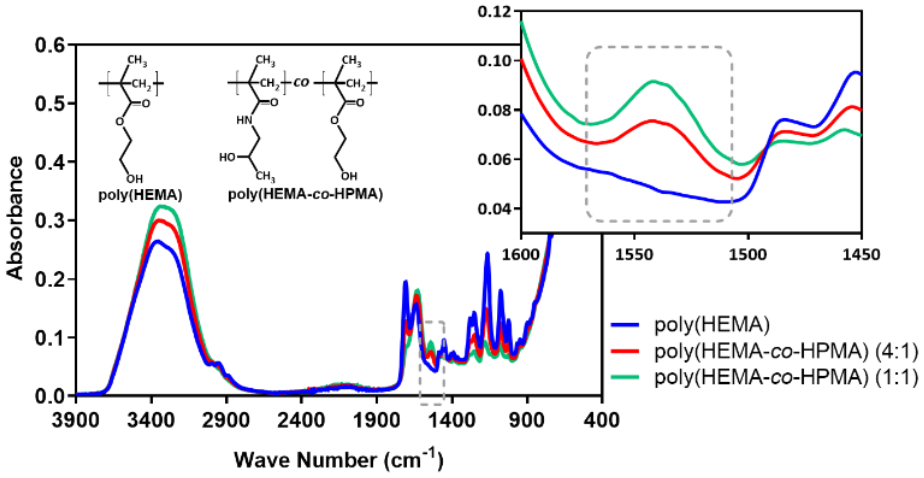

Figure 1. FTIR spectra of poly(HEMA)-based and poly(HEMA-*co*-HPMA) hydrogels at 1 mol% TEGDA showing the presence of the 2° amide.

2.3.2. DSC thermogram of poly(HEMA) and poly(HEMA-co-HPMA) at different cross-linker concentrations

The DSC thermograms of the hydrogels following application of the heating cycle are presented in **Figure 2A and B**. Each showed a broad endotherm that represented the melting of frozen water within the fully hydrated hydrogel. The occurrence of two peaks was clearly evident in both poly(HEMA) and poly(HEMA-*co*-HPMA) (4:1) at 3 mol% TEGDA cross-linker concentration. The low temperature onset of the endotherm corresponded to the start of melting of the freezable bound water followed by the melting of the freezable free water.

The melting temperatures (°C) of freezable bond water corresponded to the peak of the first Gaussian curve at lower temperature as marked on graphs in **Figure 2A and B**. An example of baseline selection and the Gaussian curve fitting to the endothermic transition is shown in **Figure 2C**.

The freezable bound water within the hydrogel interacts with the polymer backbone either directly or via other water molecules; such interaction is not strong enough to keep the water unfrozen but

does cause appreciable depression in the melting/ freezing point of the water. The rest of the freezable water is free water and has minimal or no interaction with the polymer, hence follows the thermodynamic behavior of bulk water, freezing at 0°C. Accounting for the difference in heat capacity of supercooled water, provided a more accurate estimation of freezable water content within the hydrogel. This approach accounts for the difference in the heat capacity of supercooled water and ice. There have been several attempts, both experientially [95, 96] and via mathematical modeling [97], to describe the thermodynamic behavior of supercooled water, however, the data reported by Higuchi and Iijima [46] was used in this work as it was measured in a similar polymeric system. This heat capacity was calculated from the difference in enthalpy of phase transition in poly(vinyl alcohol-co-itaconic acid) hydrogel during heating and cooling cycles and was based on the fact that the amount of water that undergoes phase transition was equal in both cycles [46, 98]. When the total water content of the hydrogel was lower, at higher cross-linker concentrations for example, the endothermic peaks attributed to the two freezable states of water were more distinctly separated as the depression in the freezing temperature of freezable bound water was higher. When the total water content of the hydrogel was higher, at lower cross-linker concentrations for example, the endothermic peaks attributed to the two freezable states of water were less distinctly separated as the depression in the freezing temperature of freezable bond water was less. Under these conditions, the peak corresponding to freezable bound water shifts towards that of freezable free water creating a broad endothermic peak around 0°C that must be deconvoluted. The peak associated with the freezable bound water moved from -6.72°C at 3 mol% TEGDA to the -0.7°C

as TEGDA decreased to 0.1 mol% TEGDA in the poly(HEMA-*co*-HPMA) (4:1) hydrogel (and correlated with the decrease in the total water content).

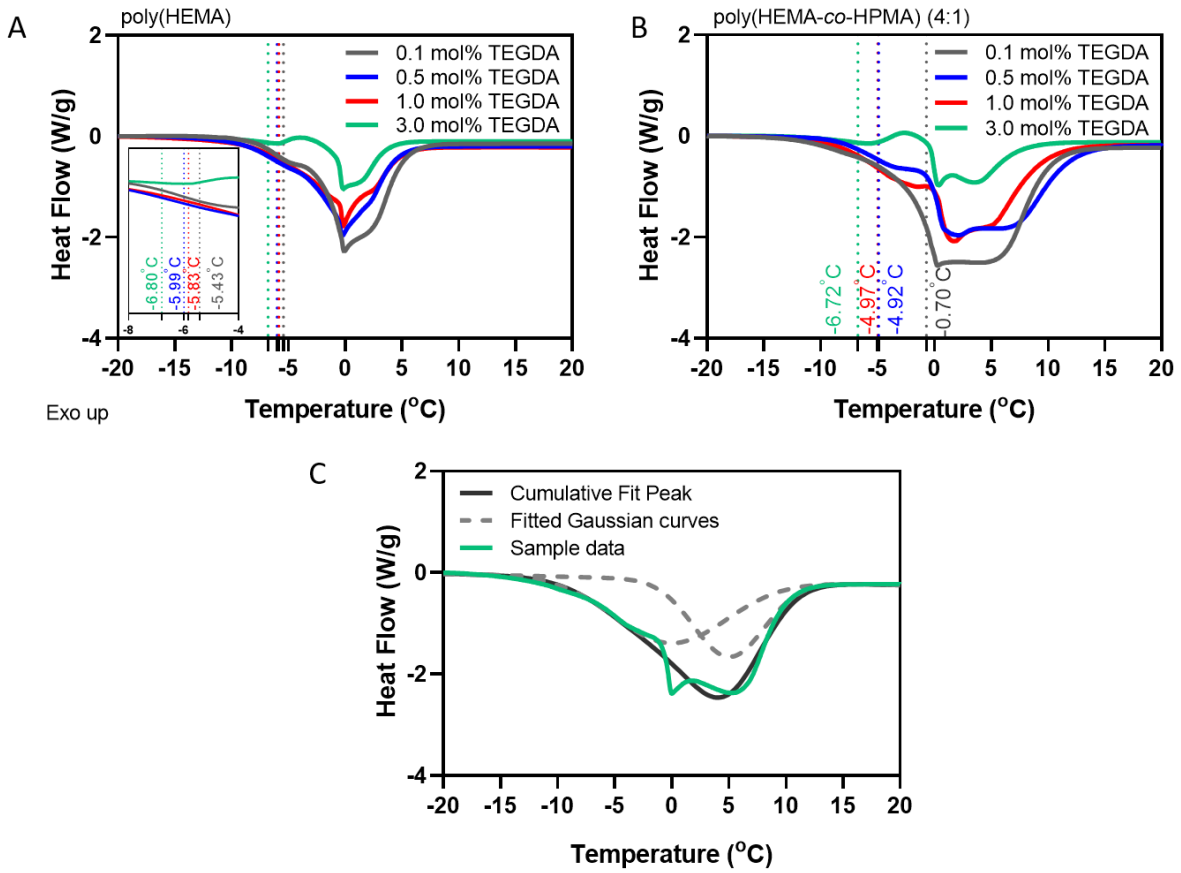

Figure 2. DSC thermograms of the variously synthesized hydrogels at and around the melting point of water. (A) poly(HEMA), (B) poly(HEMA-*co*-HPMA)(4:1) as a function of cross-linker concentrations (0.1, 0.5 1.0, and 3.0 mol% TEGDA), and (C) The Gaussian curves fitted to the endothermic transition in order to distinguish freezable bound and freezable free water.

2.3.3. Water content and water distribution of poly(HEMA) and poly(HEMA-co-HPMA) at different cross-linker concentrations

Effect of cross-linker concentration: The degree of hydration (DoH) as a function of cross-linker concentration in poly(HEMA) and poly(HEMA-*co*-HPMA) hydrogels (**Figure 3**) shows that the total water content decreases significantly ($p \leq 0.01$) as TEGDA increased from 0.1 to 3 mol% in the expected asymptotic manner. The DoH of poly(HEMA) and poly(HEMA-*co*-HPMA) (4:1)

dropped from 55% and 77% to 46% and 50%, respectively, when the TEGDA increased from 0.1 to 3 mol% with the copolymer being consistently more hydrated than poly(HEMA). Increased cross-linker impedes infinite hydrogel expansion. At lower cross-linker concentrations (0.1 - 1.0 mol%) the water was similarly distributed between freezable free and non-freezable bond water in both poly(HEMA) and poly(HEMA-co-HPMA) (4:1). Increasing the cross-linker concentration to 3 mol%, however, changed the distribution of water. In poly(HEMA), a relatively higher portion of water was allotted to non-freezable bound water and in poly(HEMA-co-HPMA) (4:1) the non-freezable bound water exceeded the freezable water (cross-linking effect). In both hydrogels and at all cross-linking densities, the freezable free water constituted the higher portion of the total freezable water. The equilibrium free water content of a hydrogel depends on the balance between the solubilization forces acting on the chemical composition the repeat units and the restrictive elastic forces of the extended polymer chains. While the freezable free water underwent considerable decrease upon an increase in the cross-linker concentration (to 3 mol%), the freezable bond water fluctuated, showing little systematic change within its generally low percentage domain. The non-freezable bound water forms because of strong hydrogen bonding between water and moieties pendant to the polymer backbone and hence is highly dependent upon the molecular composition and flexibility of pendent groups of the hydrogel.

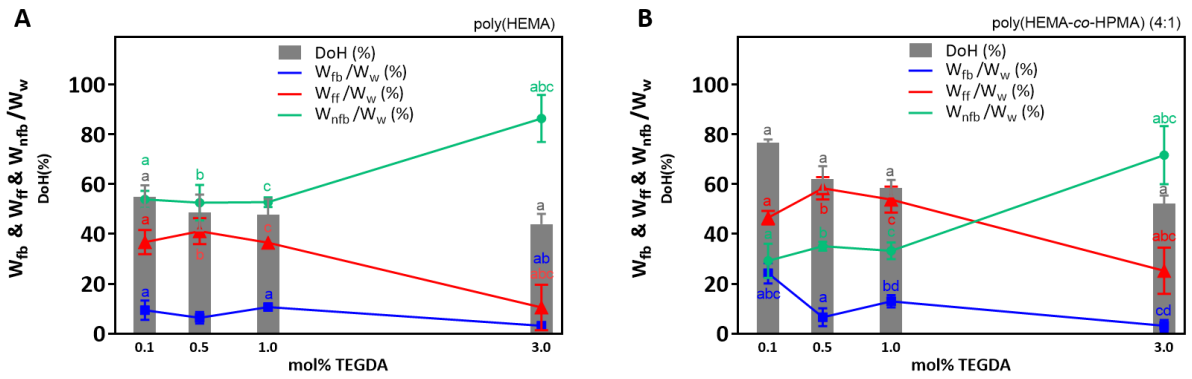

Figure 3. The degree of hydration (DoH) and the distribution among water states as a fraction of the total water content ($W_w = W_{ff} + w_{fb} + W_{nfb}$) expressed as the fraction freezable free water (W_{ff}), freezable bound water (W_{fb}), and non-freezable bound water (W_{nfb}) in the variously synthesized hydrogels (A) poly(HEMA) and (B) poly(HEMA-*co*-HPMA)(4:1) as a function of cross-linker concentrations (0.1, 0.5 1.0, and 3.0 mol% TEGDA). Pairs with similar letter are significantly different ($p \leq 0.05$).

Effect of composition: Total water content (DoH) of the poly(HPMA-co-HPMA) hydrogels was significantly higher ($p \leq 0.01$) than their poly(HEMA) counterparts all cross-linker concentrations (**Figure 3**). Using group contribution, the solubility parameters (δ) of HEMA and HPMA were calculated to be 24.66 and 27.59 $J^{1/2}/cm^{3/2}$, respectively [80]. The higher hydrophilicity of HPMA compared to HEMA is in accord with the higher water content of poly(HEMA-*co*-HPMA) (4:1). The terminal O-H group pendant to the main chain of poly(HEMA) tends to form strong hydrogen bonds with adjacent monomers and hence decreases the opportunity for penetrating water molecules to form hydrogen bonds with these groups. HPMA, on the other hand, has a flange hydrophobic methyl side group adjacent to its terminal O-H group which sterically limits the formation of hydrogen bonds with other polymer chains. The composition of the hydrogel not only changed the total water content but notably affected the distribution of water inside the hydrogels. The W_{nfb}/W_W ratio was larger than 50% for all cross-linker concentrations in poly(HEMA) but not for poly(HEMA-*co*-HPMA) (4:1) indicating that non-freezable water constituted a larger portion of total water content in the poly(HEMA) composition. The methyl group of HPMA distorts the water surrounding the hydroxyl group with possibility of forming longer hence less

strong bonds. These repelled water molecules suppress the formation of strong hydrogen bonds with O-H and hence caused a decrease in the W_{nfb} [94].

2.3.4. Glass transition temperature of poly(HEMA) and poly(HEMA-*co*-HPMA) at different cross-linker concentrations

With regards to the glass transition temperature (T_g), reflective of chain segmental mobility within the hydrogel (**Figure 4**) was not influenced by cross-linker concentrations that are studied here. Cross-linker concentration is an important factor in determining the polymer chain mobility by forming short, strong, covalently bonded segments between chains and hence directly causing an increase in T_g. [99] However, at the small cross-linker concentrations studied here, T_g was not considerably influenced. When the effect of composition on T_g was considered, poly(HEMA) had lower T_g (Avg. T_g = 101.8°C) than poly(HEMA-*co*-HPMA) (4:1) (Avg. T_g = 114.3°C). Hence, the inclusion of HPMA caused an increase in total water content, decreased the percentage of non-freezable bound water (W_{nfb}) and acted to increase T_g. The plasticizing effect of higher non-freezable bound water, W_{nfb}, in poly(HEMA) was reduced in poly(HEMA-*co*-HPMA), effectively increasing inter- and intra-chain hydrogen bonding, thus providing for less segmental mobility in the polymer, causing an increase of T_g [100]. Additionally, the 2° amide group in HPMA has less mobility compared to the acryloyl group of HEMA, which could result on an overall decrease in main chain mobility of the poly(HEMA-*co*-HPMA) (4:1) hydrogel and hence higher T_g.

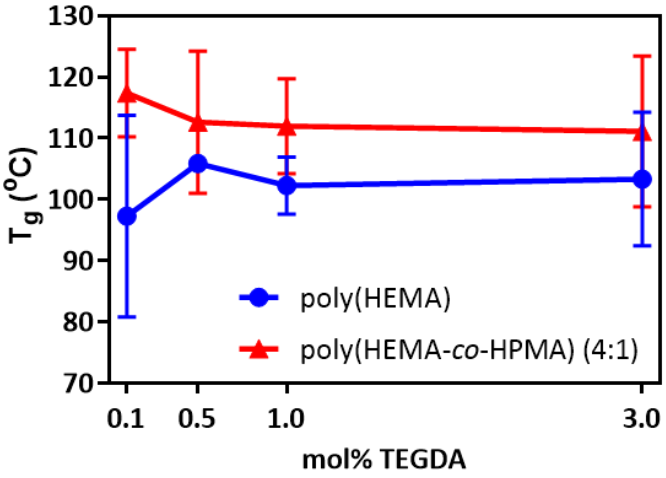

Figure 4. Glass transition temperature (T_g) of poly(HEMA) and poly(HEMA-*co*-HPMA)-based hydrogels as a function of cross–linker concentration corresponding to 0.1, 0.5, 1.0, and 3.0 mol% TEGDA cross-linker.

2.3.5. Elastic modulus of poly(HEMA) and poly(HEMA-*co*-HPMA) at different cross-linker concentrations

The elastic modulus of the various hydrogels is shown in **Figure 5**. In general, the modulus of poly(HEMA-*co*-HPMA) (4:1) was lower than its poly(HEMA) counterparts which seemed to be controlled directly by the water content of the hydrogel. The modulus increased with increasing cross-linker concentration for both hydrogels because of the resultant stiffer network. [101] The modulus of poly(HEMA-*co*-HPMA) (4:1) was more influenced by cross-linker concentration as the increase in modulus was 1.7 times larger for this hydrogel compared to poly(HEMA) when TEGDA increased from 0.1 to 3 mol%. These observations confirmed that water content and water distribution were more directly impactful on hydrogel modulus than cross-linker concentration at low to medium densities [39].

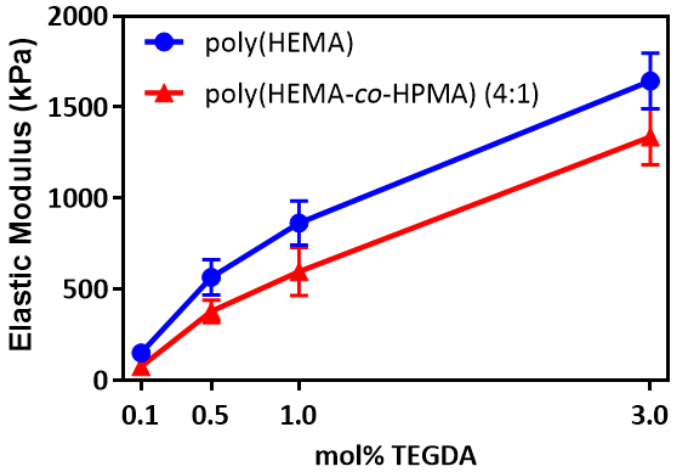

Figure 5. Elastic modulus (kPa) of poly(HEMA) and poly(HEMA-*co*-HPMA)-based hydrogels as a function of cross–linker concentration corresponding to 0.1, 0.5, 1.0, and 3.0 mol% TEGDA cross-linker.

2.3.6. Characterization of poly(HEMA-*co*-HPMA) (1:1) hydrogel

The unique formulation comprising HEMA:HPMA ratio of 1:1 (50%) was subject to further detailed characterization. The superior role of composition (addition of HPMA) over cross-linker concentration in determining general properties of these hydrogels was gleaned from the previous section. To better understand the role of composition and its effect on water content, water distribution and key biotechnical properties (void fraction, release of loaded drug, and etc.), a poly(HEMA-*co*-HPMA) hydrogel was synthesized with a 1:1 ratio of HEMA and HPMA at 1 mol% TEGDA concentration and the results were compared with poly(HEMA) and poly(HEMA-co-HPMA) (4:1) also at 1 mol% TEGDA. The FTIR analysis (**Figure 1, inset**) showed the intensity of the peak at 1530 cm^{-1} representing the 2° amide II in poly(HEMA-*co*-HPMA) (1:1) compared to (4:1) ratio, which confirmed the increase in the amount of HPMA content.

2.3.6.1. DSC thermogram, Degree of hydration, water distribution, glass transition temperature, and elastic modulus

When the cross-linker concentration was kept constant (1 mol% TEGDA) and the effect of addition of HPMA was considered, addition of 20% HPMA to poly(HEMA) changed the water distribution (composition effect) (**Figure 6**). The melting point of freezable bound water, $T(W_{fb})$, was progressively increased when the total water content of the hydrogel was increased [47]. The melting point of freezable bound water was about -5.83°C in poly(HEMA) and -4.97°C in poly(HEMA-*co*-HPMA) (4:1) which increased to -1.53°C when the HPMA content was further increased in poly(HEMA-*co*-HPMA) (1:1) (**Figure 6A**). This shift indicated that the water that occupied the interphase between strongly polymer-bonded, non-freezable bound water and freezable free water became weaker and progressively more similar to bulk water as the HPMA content was increased. Replacing 20% of HEMA in poly(HEMA) with HPMA in poly(HEMA-*co*-HMPA) (4:1) hydrogel likewise changed the distribution of water such that the non-freezable bound water content was reduced to a lower percentage than that of freezable water. The majority of water in poly(HEMA) was strongly bonded to the polymer backbone as non-freezable bound water while addition of amphiphilic HPMA monomer altered water distribution within the hydrogel. Further increase of HPMA (50%) (1:1) did not appreciably change the non-freezable bound water content within the hydrogel. The elastic modulus went from 8.64 ± 1.21 kPa to 5.04 ± 0.44 kPa in going from 1:0 to 1:1 HEMA:HPMA ratio (45% decrease). The free water content was similarly higher for the hydrogel with larger HPMA content. The W_f content went from 40.86 ± 3.18 to 68.44 ± 5.03 in going from 1:0 to 1:1 HEMA:HPMA ratio (40% increase). The glass

transition temperature, T_g, on the other hand, did not change appreciably showing only a modest trend upward (+7°C or +15%) with introduction of HPMA.

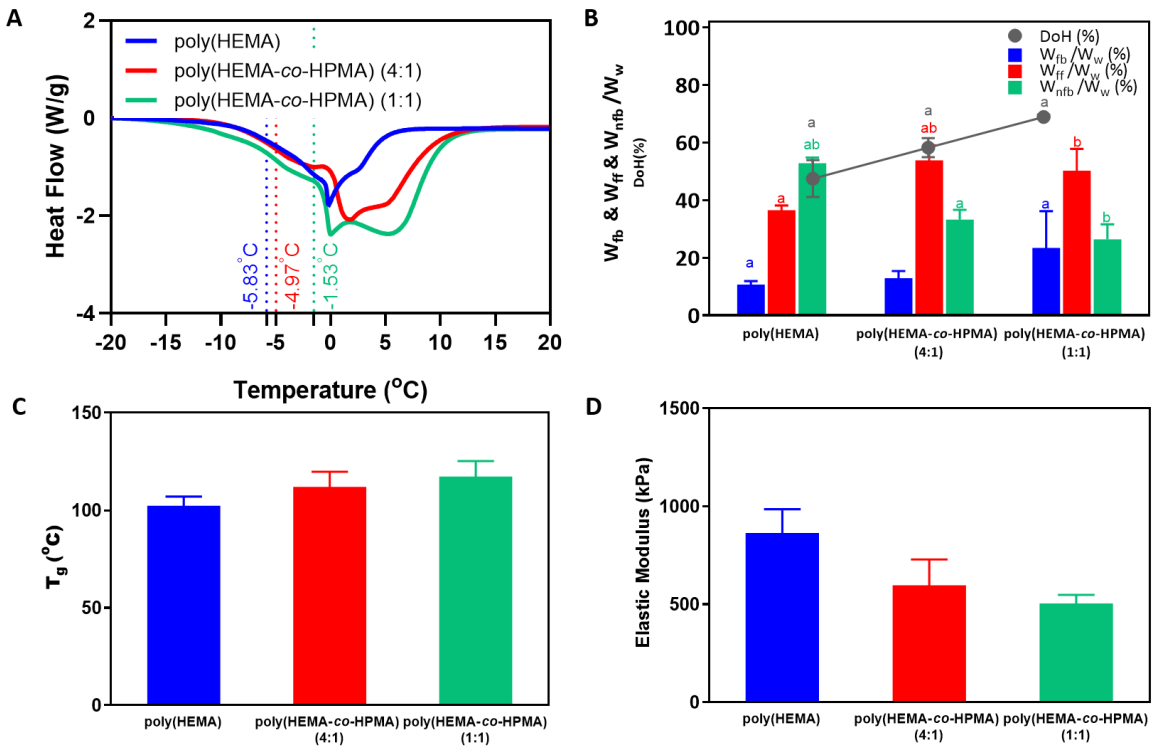

Figure 6. (A) DSC thermograms at and around the melting point of water, (The freezing temperatures of freezable bound water (W_{fb}) have been marked as dotted lines on the graphs), (B) Degree of hydration (DoH %) and distribution among water states as a fraction of the total water content ($W_w = W_{ff} + w_{fb} + W_{nfb}$) expressed as the fraction freezable free water (W_{ff}), freezable bound water (W_{fb}), and non-freezable bound water (W_{nfb}), (C) elastic modulus, and (D) glass transition temperature , T_g, of poly(HEMA), poly(HEMA-*co*-HPMA) (4:1), and poly(HEMA-co-HPMA) (1:1) at 1 mol% TEGDA cross-linker. n= 3. Pairs with similar letter are significantly different ($p \leq 0.05$).

2.3.6.2. SEM and void fraction

The results of void fraction calculation showed that poly(HEMA-*co*-HPMA) (1:1) had the highest fraction of void cavities (65%) when compared to the other two compositions (**Table 2**). The SEM images (**Figure 7**) show visible differences in the freeze-fractured surface roughness of the three compositions with the poly(HEMA-*co*-HPMA) (1:1) showing the highest surface roughness. The SEM technique does not give conclusive information about the pore size of the hydrogel as

hydrogels have generally homogenous microstructure with nano-sized pores. However, since the SEM images were collected from freeze-fractured cross-sections, the overall roughness of the surface relates to the size of freezable ice domains formed inside the hydrogel mesh. The higher water content of the poly(HEMA-*co*-HPMA) (1:1) was well reflected in the void fraction and SEM data, as both showed higher void cavities and larger pore size of this composition, resulting from the increased size of water packets within the hydrogel.

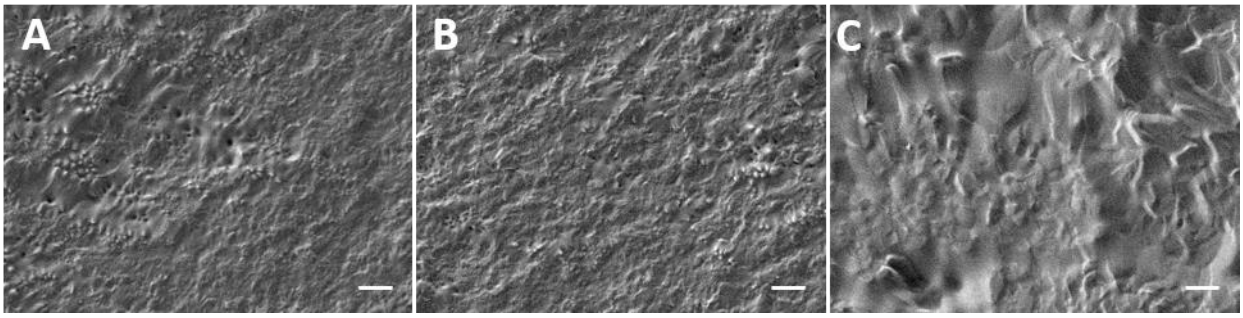

Figure 7. SEM image (X1000, 5.0 kV) of freeze-fractured cross section of (A) poly(HEMA), (B) poly(HEMA-co-HPMA) (4:1), and (C) poly(HEMA-*co*-HPMA) (1:1) at 1 mol% TEGDA cross-linker. Scale bar shows 10 µm.

Table 2. Root mean square surface roughness (R_q) and void fraction (ε) of poly(HEMA), poly(HEMA-*co*-HPMA) (4:1), and poly(HEMA-*co*-HPMA) (1:1) at 1 mol% TEGDA cross-linker.

	R_q (µm)	Void Fraction% (ε)
poly(HEMA)	11.58	45.57 ± 0.84
poly(HEMA-co-HPMA) (4:1)	11.99	57.13 ± 1.54
poly(HEMA-co-HPMA) (1:1)	16.07	64.94 ± 2.99

2.3.6.3. Swelling kinetics of the hydrogel

Figure 8 presents the fraction of mass gain of hydrogels during swelling. The rate at which a hydrogel imbibes water is reflected in its swelling kinetics. The initial water uptake rates, the slope of the relative mass of absorbed water to dried hydrogel at time *t* during the first 30 min of the swelling, showed that poly(HEMA-*co*-HPMA) (1:1) absorbed water three times faster than poly(HEMA). Interestingly, when the time was considered, the poly(HEMA) was shown to have the fastest hydration as its time constant was ~16% less of the HPMA-containing hydrogels.

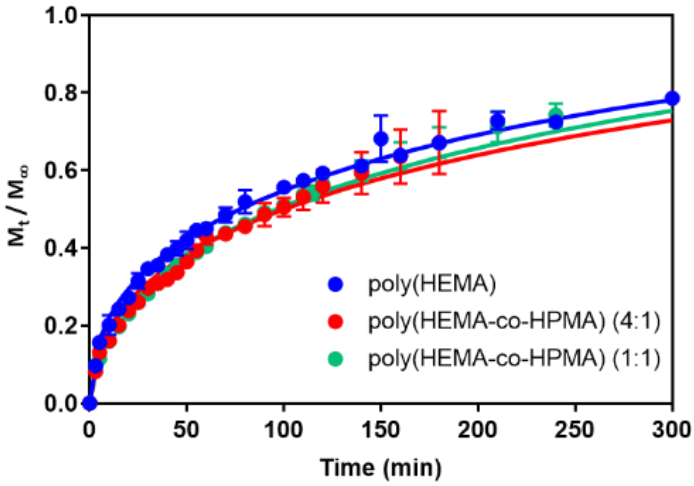

Figure 8. Normalized swelling kinetics of poly(HEMA), poly(HEMA-*co*-HPMA) (4:1), and poly(HEMA-co-HPMA) (1:1) at 1 mol% TEGDA cross-linker measured by gravimetric technique.

The normalized swelling graphs and mathematical model fitting [88] using equation 7 to describe the transport mechanism of water/ion during swelling are summarized in **Table 3**. The diffusional exponent, *n*, shows the swelling of the three compositions follow a Fickian model and are controlled by rate of water diffusion into the hydrogel. The exponential constant depends on the aspect ratio of the hydrogel; which for a cylinder, *n*=0.45 describes a purely Fickian diffusion transport and occurs when the penetration rate of water is smaller relative to the rate of polymer chain relaxation [85, 102]. Deviation from 0.45 to higher values ($0.45 < n < 0.89$) represents a trend

towards an anomalous transport phenomenon which occurs when the water diffusion is comparable to the polymer chain relaxation rate. The pre-exponential coefficient, *k*, was highest in poly(HEMA) reflecting the fastest swelling rate. Both the reduced values of *k* and deviation from *n*=0.45 suggested an anomalous transport of water into the HPMA-containing hydrogels that was likely the result of the lower non-freezable bound water which made a slower relaxation of chain segments due to inter- and intra-chain hydrogen bonding [103].

Table 3. The values of k and n extracted from model fitting of swelling kinetic data from poly(HEMA), poly(HEMA-co-HPMA) (4:1), and poly(HEMA-co-HPMA) (1:1) at 1 mol% TEGDA cross-linker

	Initial water uptake rate ($g_w g_{dH}^{-1} h^{-1}$)	Total water uptake/mass of dry hydrogel	Time constant of swelling (min)	K^n	
				K (min^{-n})	n
Poly(HEMA)	0.56	%70	150	0.073 ± 0.018	0.44 ± 0.09
Poly(HEMA-*co*-HPMA) (4:1)	0.88	%130	190	0.059 ± 0.004	0.47 ± 0.03
Poly(HEMA-*co*-HPMA) (1:1)	1.58	%240	180	0.054 ± 0.006	0.49 ± 0.03

2.3.6.4. Release of FITC-labeled dextran

Hydrogels are frequently used in the fashioning of drug delivery systems to release bioactives, e.g. growth factors, and other small molecules from a substrate or scaffold to cells in culture or *in vivo* [101, 104]. To this end, the release of 40kDa FITC-Dextran (a drug surrogate) loaded and entrapped within the cross-linked hydrogels and its inferred transport mechanism were studied. The fractional FITC-dextran that was released from the hydrogel showed a dramatic difference of the release profile amongst the three hydrogels (**Figure 9)**.

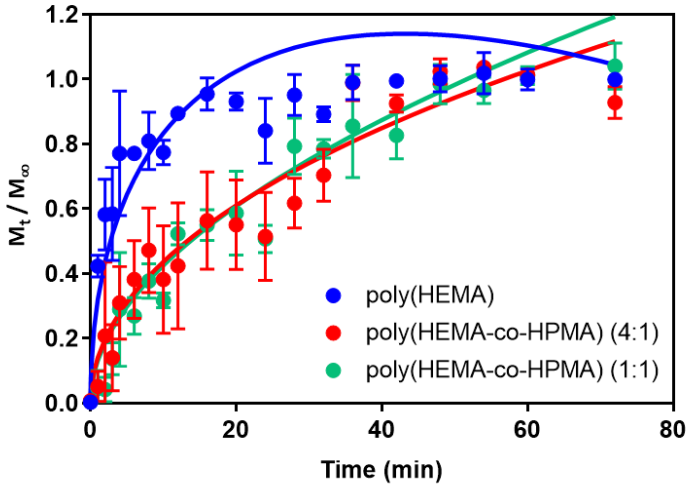

Figure 9 Release profiles of FITC- dextran (40 kDa) from poly(HEMA), poly(HEMA-co-HPMA) (4:1), and poly(HEMA-*co*-HPMA) (1:1) at 1 mol% TEGDA cross-linker.

Dextran showed a rapid burst release from poly(HEMA) as it took 3.5 h for 63.2% of the molecule (23 µg/mL) to be released. [105] This was followed by a slow release which stabilized after 36 h. The initial release from poly(HEMA-*co*-HPMA) (4:1) and poly(HEMA-*co*-HPMA) (1:1) took place at a gentler rate and reached the targeted 63.2% (5.8 and 9.1 µg/mL, respectively) in ~26 h and stabilized after 48 h. Both early and late diffusion coefficients (calculated according to equations 8 and 9, respectively) were an order of magnitude larger for poly (HEMA) (D_E = 2.16 x 10^{-8} m^2 s^{-1}) compared to the HPMA-containing hydrogels (D_E ~ 0.20 x 10^{-8} m^2 s^{-1}). These values were in accordance with the swelling rate, which was the fastest for poly(HEMA) and showed the FITC-dextran diffusion from the hydrogel to be in countercurrent with the diffusion of water. The lower early (D_E) *vs.* late (D_L) diffusional constant for poly(HEMA) reflected a compromise of diffusivity over time. However, this trend was reversed in the HPMA-containing hydrogels which showed an increase in diffusivity over time. As the polymer network matrix swells, the concentration gradient changes and so does the diffusivity of the releasable factor. The water that diffuses into the hydrogel and hydrogen bonds to the HEMA and HPMA repeat units reduces inter-

and intra-chain hydrogen bonding interactions and effectively opens pores within the mesh. It also decreases the resistance to diffusion and facilitates/accelerates the diffusion. In addition to the fast release, the cumulative amount of the dextran released from the poly(HEMA) was 30 µg/mL and was approximately three times higher than for the other two hydrogels (8.8 and 14 µg/mL).

To gain insight into the role of composition on factor transport mechanism, the data was fitted to the empirical equation 7 and the exponential and kinetic constants were extracted. The value *n* was found to be largest for poly(HEMA-*co*-HPMA) (1:1) (n = 0.58) indicating anomalous transport with appreciable factor-polymer interaction or relaxation influence. To evaluate the relative contributions to anomalous diffusion equation 10 was applied. The k_1 release constant, representing dextran/hydrogel interactions, decreased with increasing HPMA content confirming increased factor-to-hydrogel interactions with increasing HPMA content. The k_2 constant which describes the influence of polymer relaxation, was lowest for poly(HEMA) and increased with increasing HPMA content confirming less dynamical chain segments consistent with a higher T_g and less non-freezable bound water in the HPMA hydrogels. The overall larger values of k_1 compared to k_2 showed the predominant influence of factor diffusion on the release profile of dextran.

Table 4. The kinetic of total FITC-dextran released from the poly(HEMA), poly(HEMA-co-HPMA) (4:1), and poly(HEMA-co-HPMA) (1:1) at 1 mol% TEGDA cross-linker.

	Total release (µg/ mL)	Time Constant, τ (h)	D_E(x 10^{-8}) m^2 s^{-1}	D_L(x 10^{-8}) m^2 s^{-1}	$M_t/M_\infty = kt^n$				$M_t/M_\infty = k_1 t^{0.5} + k_2 t$			
					k (x 10^{-2}) (h^{-n})	n	Adjusted R^2	SSE (x 10^{-2})	k_1 (x 10^{-2}) ($h^{-0.5}$)	k_2 (x 10^{-4}) (h^{-1})	Adjusted R^2	SSE (x 10^{-2})
Poly(HEMA)	0.31	3.5	2.16	1.19	7.4	0.41	0.96	0.82	7	≈ 0	0.98	0. 44
Poly(HEMA-*co*-HPMA) (4:1)	0.88	28	0.19	0.37	2.3	0.44	0.88	4.65	2	≈ 0	0.89	4.23
Poly(HEMA-*co*-HPMA) (1:1)	0.14	26	0.22	0.32	0.88	0.58	0.89	5.55	1	0.7	0.88	5.86

2.3.7. Correlation analysis

Table 5 summarizes the results of the correlation analysis between total water content (DoH), water distribution and the biotechnical properties of poly(HEMA-co-HPMA) hydrogels explored as a function of HEMA:HPMA composition ratio. The first three rows present the correlation coefficients for the ratio of the various components relative to the total water content. The fourth row explores the ratio of total freezable water ($W_f = W_{ff} + W_{fb}$) to total hydration. The final three rows explore the ratio of the various components relative to the non-freezable bound water content. The results show that within the freezable water content (W_f), it was the freezable free (W_{ff}) portion which most influenced the swelling and release profile of the hydrogel. The freezable bound (W_{fb}) portion of water had no significant correlation with the properties measured in this study. The highest correlation, though, was revealed for the non-freezable bound water (W_{nfb}) as this is the

portion of imbibed water that strongly interacts with the polymer, hence it influences the hydrogel's response at the molecular level. Moreover, it is the abundance of freezable water relative to total water (W_f/W_W) (row 4 of **Table 5**) and of this, the freezable free water relative to the non-freezable bound water (W_{ff}/W_{nfb}) (row 6 of **Table 5**) that most influences biotechnical properties. This detailed analysis therefore adds no further insight than can be gleaned for treating all water as freezable water and non-freezable bound water. The elastic modulus was shown to be anti-correlated with both the degree of hydration (DoH) and the freezable water content (W_f/W_w), consistent with intuition and established hydrogel theory [106]. The stronger correlation of elastic modulus with water distribution suggests the importance of the plasticizing effect of bound water on this important biotechnical property. T_g did not show significant correlation with either water content or water distribution. The strong positive correlation of void fraction and surface roughness with the DoH, was evidence that indeed the gross surface roughness might arise from deformations associated with the freeze-facture of water packets within the hydrogel.

Both time constants for swelling and dextran release, diffusion dominated phenomena, showed stronger correlation with water distribution than with water content. The two properties were simultaneously negatively correlated with non-freezable bound water suggesting that an increase in the non-freezable portion of water (an equilibrium value) was associated with faster swelling of the hydrogel and faster release of dextran through a decrease in their time constants (a kinetic value). The parallels in the correlations of these two kinetic parameters with water content and distribution (equilibrium parameters) are noteworthy particularly in view of the fact that $\boldsymbol{\tau}$ for swelling is in minutes and $\boldsymbol{\tau}$ for release is in hours. The loaded dextran likely forms virtual bonds with the polymer chains which become displaced by tightly bound water. As the small water molecules enter the hydrogel, they bind to the chains and replace the dextran hence free this

molecule to diffuse out of the hydrogel. This phenomenon along with the opening of the hydrogel mesh following water penetration causes the dextran to diffuse out of the hydrogel.

Table 5. Pairwise correlation coefficients established between the multiple states of water and the key biotechnical properties of poly(HEMA-*co*-HPMA)-based hydrogels. The asterisk * and double asterisk ** show p < 0.05 and <0.01, respectively.

	Elastic modulus (kPa)	Glass transition temperature (Tg (℃))	Void fraction (ε)	Freeze fracture surface roughness (Rq (μm))	Time constant of swelling (τ (min))	Time constant of release of FITC-dextran (40 kDa) (τ (h))
W_{fb}/W_W	-0.45	0.37	0.56	0.71	0.30	0.41
W_{ff}/W_W	-0.66	0.49	0.70	0.28	0.84*	0.84*
W_{nfb}/W_W	0.83**	-0.61	-0.90**	-0.69	-0.82*	-0.90**
W_f/W_W	-0.83**	0.61	0.90**	0.69	0.82*	0.90**
W_{fb}/W_{nfb}	-0.48	0.33	0.59	0.75	0.33	0.44
W_{ff}/W_{nfb}	-0.79*	0.55	0.87*	0.66	0.81*	0.88**
W_f/W_{nfb}	-0.74*	0.50	0.83*	0.77*	0.66	0.76*

2.4. Conclusions

This study reported on the importance of water distribution within hydrogels, its dependence on cross-linker concentration and monomer composition, and its impact on key biotechnical properties. Over the range studied (0.1 to 3.0 mol% TEGDA), increased cross-linker concentration increased the elastic modulus and non-freezable water, and decreased the degree of hydration, decreased the freezable water content but did not change the T_g. The addition of the more water soluble, amphipathic monomer, HPMA, to the poly(HEMA)-based hydrogel transformed the hydrogen bonding in the polymer by decreasing the possibility of formation of strong hydrogen bonds between water and the polymer and this served to increase the total hydration and freezable

fraction at the expense of the non-freezable bound water content. The increase in total water content (DoH) led to a network with higher void fraction while the decrease in non-freezable bound water resulted in a slight increase in T_g. The presence of HPMA at any level caused a modest increase in the swelling time constant. FITC-dextran was released from the amphipathic poly(HEMA-*co*-HPMA) with a gentler profile while a burst-style release profile was obtained from poly(HEMA)-based hydrogels. Correlation analysis confirmed that an increase in non-freezable bound water was related to a decrease in the time constant for both swelling and release and confirmed that equilibrium water distribution was more important than DoH in correlation with these kinetic parameters. The total freezable water ($W_{fb} + W_{ff}$) as a fraction of total water was highly correlated (and its correspondent, non-freezable bound water, anti-correlated) with key biotechnical performance characteristics of the hydrogels. Of the two deconvoluted components of freezable water, freezable free water was most influential on the properties studied. The two components of the freezable water act cooperatively and in concert when influencing properties and are more important than the total water content of the hydrogel. The ratio of freezable free water to non-freezable bound water (W_{ff}/W_{nfb}) is equally strongly correlated with key biotechnical performance characteristics of the hydrogels. The hydrogen bonds formed by water molecules with the polymer network influenced their thermodynamic behavior which is reflected in the endothermic peak of the DSC thermogram and corroborated by FTIR analysis. The results of this report indicate that the water distribution should not be overlooked when the hydrogel's biotechnical performance is being studied and is a tunable feature when engineering hydrogel performance.

3. BIODEGRADATION AND RELEASE FROM BIOHYBRID POLY(GELMA-*CO*-HEMA-*CO*- HPMA) HYDROGELS

3.1.Introduction

Cardiovascular tissue and regenerative engineering scaffolds demand thorough understanding of angiogenesis as it is one of the essential processes of successful tissue formation. Endothelial cells (EC), as the building blocks of blood vessels, are consequently important in understanding scaffold–cell interactions. The evolving view of a scaffold has shifted from an implantable (permanent) bio-benign material for the support of growing and proliferating cells to a temporary, biologically responsive, indwelling material capable of the recruitment of a plurality of cells to support and guide tissue innervation [1, 2] and angiogenesis [3]. Degradable scaffolds, a class of bioresponsive polymers, endow some level of plasticity through remodeling to the growing cells/ tissue and hence have become very popular in tissue engineering and regenerative medicine applications [4-6]. Enzymatically degradable scaffolds are designed mostly using natural polymers, including extracellular matrix (ECM) proteins, and/or peptides derived from them, that contain specific amino acid sequences cleavable by proteases or that serve as biochemical cues for the recruitment and attachment of cells. Incorporation of such motifs within the scaffold causes it to degrade upon exposure to specific proteolytic enzymes [7]. Such approaches have been successfully used to engineer a responsive scaffold for cells that allows cells to rebuild the scaffold with their own extracellular matrix or to provide on-demand drug delivery [8].

To confer enzymatic degradability, natural polymers, e.g. gelatin, or cleavable synthetic peptides may be embedded within the polymer's native network architecture. Peptides could be designed to provide highly specific enzyme response, however, despite being elegant, their synthesis requires specialized tools and expertise and so demand a high investment. Using pure natural

polymers, on the other hand, may compromise controllability and/or may initiate immune response while modification of their chemistry might not be always a viable option. Therefore, the need for a more accessible option has not been met. One option is the natural-synthetic biohybrid polymer scaffold. Natural-synthetic biohybrid polymers are synthesized from natural polymers such as gelatin and synthetic monomers such as 2-hydroxyethylmethacrylate (HEMA) and N-(2-Hydroxypropyl) methacrylamide (HPMA) to yield poly(GelMA-*co*-HEMA-*co*-HPMA) as cross-linked, polymeric hydrogels.

Gelatin is a component of collagen, one of the abundant, easily isolatable ECM proteins, hence it contains active sites of collagen and is a good candidate for scaffold development. Gelatin introduces cleavable motifs such as to confer degradability to the polymer that contains this natural polymer. Its ready availability, low cost and ease of functionalization has resulted in gelatin becoming a popular option for development of biodegradable scaffolds [9-11]. The native origin of gelatin influences its amino acid composition which subsequently determined the molecular weight and gel strength of the polypeptide [12]. The molecular weight of gelatin at 35 °C has been given as 61,500 [13] but is found to be highly variable being up to 100kDa in some references [14]. Methacrylation of gelatin is possible though an inexpensive straightforward reaction with methacrylic anhydride that renders it a photo-crosslinkable polymer or macromer called GelMA [15, 16]. In this process, some or all of the free amine groups of the gelatin molecule are replaced with acryloyl groups. Having several acryloyl on a molecule, GelMA can form a chemically crosslinked polymer by itself. GelMA hydrogels have been synthesized and used to accommodate different types of cells and affect cellular behavior including fate determination [17, 18]. The increasing concentration of GelMA in hydrogel was shown to enhance the cell proliferation and support differentiation of encapsulated keratinocyte cells [19].

Biohybrid, natural-synthetic polymer scaffolds synthesized from methacrylated gelatin and the synthetic monomers, HEMA and HPMA, to yield poly(GelMA-*co*-HEMA-*co*-HPMA) as cross-linked, polymeric hydrogels offer the following advantages. Gelatin confers biodegradability to the biohybrid polymer, rendering it responsive to ECM proteases in the release of loaded factors. HPMA confers a high degree of hydration but is expensive. Similar degrees of hydration may be achieved with co-polymers of HEMA and HPMA, HEMA being less expensive [20]. Due to their highly hydrophilic nature, most synthetic hydrogels, such as poly(HEMA-*co*-HPMA), resist protein adsorption and hence resist integrin mediated attachment of cells. The inclusion of gelatin promotes receptor-mediated attachment to motifs such as the cell-adhesive tripeptide, Arg-Gly-Asp (RGD) and other cell-attachment and cueing motifs such as Ile-Lys-Val-Ala-Val (IKVAV). Exactly how much gelatin is actually needed to confer the natural polymer effect/influence remains a question. Finally, all synthetic polymers may be precisely controlled, being of known molecular weight and degree of polymerization. Natural polymers, such as gelatin, being from highly variable sources are likewise highly variable in properties because of variations in exact amino acid sequence, MW and possible crosslinking. Engineering the composition of poly(GelMA-*co*-HEMA-*co*-HPMA) for effective recruitment of cells and degradative release of factors is the principal focus of this paper.

Vascular endothelial growth factor (VEGF) is a dimeric glycoprotein of MW 34 to 45 kDa wherein the monomers are bonded via disulfide bonds [21]. VEGF is a signaling protein expressed by cells generally during formation of any tissue and serve to regulate angiogenesis and vasculogensis processes [21, 22]. Its concentration in serum of a healthy individuals is about 0.2 ng/mL [23]. In endothelial cells, VEGF binds to VEGFR (receptor) on the cell membrane and promotes proliferation and migration of these cells [24]. Because of dose-sensitivity of cellular response to

VEGF [25], the release and delivery of this growth factor has been the subject of research for years [26, 27]. Ideally, a cell-demanded release is sought where the growth factor would be provided where and when it was required [7]. To this end the growth factor has been physically or covalently loaded into carriers and subsequently released in response to stimuli received from the environment; as simple as a solvent diffusion or as complex as enzymes. Diffusion based release follows Fick's second law equation. 11.

$$\frac{\partial \varphi}{\partial t} = D\ \frac{\partial^2 \varphi}{\partial t^2} \tag{11}$$

An analytical solution to this equation for films with thickness of δ under sink conditions follows equation 12.

$$\frac{M_t}{M_\infty} = 4\left(\frac{Dt}{\delta^2}\right)^{1/2}\left\{\pi^{-1/2} + 2\sum_{n=1}^{\infty}(-1)^n ierfc\frac{n\delta}{\sqrt{Dt}}\right\} \tag{12}$$

Mt and M∞ refer to the amount of factor released at time t and ∞, respectively. An estimation of this equation at early time (Mt /M∞<63%) is given by equation 13.

$$\frac{M_t}{M_\infty} = 4\left(\frac{Dt}{\pi\delta^2}\right)^{\frac{1}{2}} = K'\sqrt{t} \tag{13}$$

Where k' is a constant under assumption of constant diffusivity and unchanged film thickness [28]. To consider the effect of polymer chain relaxation on the release of factor, Peppas and Sahlin suggested the model of equation 14 [29]:

$$\frac{M_t}{M_\infty} = k_1 t^{0.5} + k_2\, t \tag{14}$$

In this equation, k_1 accounts for the diffusion-controlled release and k_2 accounts for the segmental relaxation of polymer chains, both of which are temperature dependent.

Equation 7 could be re-written as equation 15 and 16 in case of dextran being released from hydrogel considering the effect of Fickian diffusion and polymer relaxation:

$$\frac{M_t}{M_\infty} = k_1 t^{0.5} + k_2\, t = D_{eff,Dextran} t^{0.5} - D_{eff,relaxation}\, t \tag{15}$$

$$\frac{M_t}{M_\infty} = 4\left(\frac{D'_{eff,Dextran}}{\pi R^2}\right)^{0.5} t^{0.5} - D_{eff,relaxation}\, t \quad (16)$$

In the case of a degradable hydrogel, if the degradation occurs as a result of the cleavage of peptide/ polypeptides by an enzyme (proteolysis), it may be assumed to follow Michaelis-Menten kinetics for which equations 17 and 18 apply.

$$[S] + [E] \leftrightarrows [S^*E] \rightarrow [P] + [S] \quad (17)$$

$$\frac{d[P]}{dt} = v = \frac{V_{max}\,[S]}{K_M + [S]} \quad (18)$$

The numerical solution to the set of differential equations to describe the kinetic response follows the format of a Lambert W function.

$$[S]_t = K_M . W\{F(t)\} \quad (19)$$

$$F(t) = \frac{[S]_0}{K_M} \exp\left(\frac{[S]_0}{K_M} - \frac{V_{max}}{K_M}\, t\right) \quad (20)$$

Under certain conditions, the response can be simplified to equations 21 and 22 [30].

$$\frac{[S]_t}{[S]_0} = \exp\left(-\frac{V_{max}}{K_M}\, t\right) \quad \text{if} \quad [S] << K_M \quad (21)$$

$$\frac{[S]_t}{[S]_0} = -\frac{V_{max}}{K_M}\, t \quad \text{if} \quad [S] >> K_M \quad (22)$$

These models enable studying the degradation and release of payload from within an enzymatically degrading polymeric hydrogel which gives a mathematical insight into the design of scaffold/ delivery vehicle for an optimum response.

In a previous study we reported the synthesis of poly(HEMA-*co*-HPMA) hydrogels with high water content and low elastic modulus [20, 31]. In that study the crosslinker concentration and percentage of HPMA was used to tune the physiochemical and mechanical characteristics of the hydrogel. The present study reports incorporating GelMA into poly(HEMA-*co*-HPMA) with the intent of 1) providing active motifs for cell attachment, 2) enabling proteinase degradation of the hydrogel, and 3) promoting paracrine-like release of factors. The degradation of poly(GelMA-*co*-

HEMA-*co*-HPMA) in the presence of collagenase and the release of FITC-dextran (40 kDa), a surrogate of VEGF, a growth factor surrogate is studied with mathematical models describing the diffusion- and/or degradation-controlled release of the payload. The growth of human umbilical vein endothelial cells (HUVECs) on VEGF-containing poly(HEMA-*co*-HPMA-*co*-GelMA) was also investigated..

3.2. Materials and Methods

3.2.1. Materials

The 2-hydroxyethylmethacrylate (HEMA), N-(2-Hydroxypropyl) methacrylamide (HPMA), N-Tris(hydroxymethyl)methyl]acrylamide (HMMA), poly(ethylene glycol) monomethacrylate (PEG(360)MA), tetra(ethylene glycol)diacrylate (TEGDA), poly(N-vinylpyrrolidone) (pNVP) (MW=1.3M), Lithium phenyl-2,4,6-trimethylbenzoylphosphinate (LAP), gelatin (from porcine skin, del strength 300 g Bloom, type A) octadecyltrichlorosilane (OTS) and Fluorescein isothiocyanate–dextran (average MW 40,000) were purchased from Sigma Aldrich (St. Louis, MO). Antibiotic Antimycotic Solution (100×) was purchased from Sigma. For in-vitro study, primary Human Umbilical Vein Endothelial Cells (HUVECs, neonatal, pooled, 200P-05N), Endothelial Cell Growth Medium, Penicillin-Streptomycin, Trypsin-EDTA and trypsin inhibitor were obtained from Sigma-Aldrich. Rhodamine-phalloidin and DAPI were purchased from Thermo Fisher Scientific (Waltham, MA). Collagenase, type 2 was purchased from Worthington Biochemical Corporation (Lakewood, NJ). Cell culture inserts with pore size of 0.4 μm purchased from Corning, Millipore (MA).

3.2.2. Hydrogel Synthesis

Methacrylated gelatin (GelMA) was synthesized according to previously described protocol [1]. Briefly, gelatin was reacted with methacrylic anhydride (Sigma Aldrich) at 1.25 ratio followed by

dialysis and lyophilization. The degree of methcarylation was measured to be 62% using a colorimetric assay based on 2,4,6-trinitrobenzenesulfonic acid [2]. Hydrogel cocktails were prepared based on mol% of functional repeat unit. The syntenic component of the biohybrid hydrogel comprised HEMA:HPMA (1:1 mol ratio), PEGMA (5 mol%), TEGDA (0.5 mol%), HMMA (5 mol%), pNVP (viscosity modifier) (2 mol%), LAP (biocompatible photoinitiator) (0.5 mol%). GelMA was added to the cocktail based on mol% achieved by taking an amino acid sequence containing a methacrylate moiety (62% methacrylation) as repeat unit (approximated to be MW=1334 g/mol). The ratio of GelMA was changed by adjusting the concentration of HEMA:HPMA as main monomers while always maintaining the 1:1 ratio. GelMA concentrations of 0.1 and 1.0 mol% (low), 5, 10, and 15 mol% (medium), and 20, 30, 50, 70, and 87 mol% (high) were explored. All chemicals were dissolved in DI water by extended stirring. After being mixed, hydrogel cocktails were nitrogen purged and molded into disks (φ= 4.5 mm and T= 1.6mm) using silicone isolators (Grace Biolabs) followed by 150s UV exposure (UV Crosslinker) which ensured complete cross-linking. Subsequently, hydrogels were gradually hydrated by sequential immersion in ethanol/ DI water mixtures and equilibrated in DI water for all characterizations except for those related enzyme mediated release and in-vitro cell culture studies.

3.2.3. Hydrogel characterization

Hydrated hydrogels were equilibrated in 0.1M PBS (pH=7.4) before all measurements. The degree of hydration was calculated as the difference of hydrated mass in hydrated and dry forms divided by the hydrated mass [78]. Compressive modulus was measured in compression extension mode with an Instron 3345 (Norwood, MA) a 0.1 N pre-load up to 10% strain [83].

3.2.4. Degradation and release profile of hydrogels

The degradation rate of biohybrid hydrogels was determined from cumulative mass loss of the immersed hydrogel disks. The release rate of FITC-Dextran 40kDa was determined from cumulative increase in fluorescence intensity of the bathing solution within which the hydrogel disk was immersed. Both degradation and release were studied at 37 °C in 0.1M PBS (pH=7.4) and in 0.1M PBS (pH=7.4) containing the enzyme collagenase. For degradation studies, hydrogel disks (φ=4.5 mm and T=1.6 mm) were lyophilized for obtaining the initial dry mass. The dried disks were then fully equilibrated in PBS buffer before the test (overnight). Hydrogels were then incubated in either PBS as control or PBS containing 400 μL of 2.5 U/mL collagenase type II and kept in a shaking water bath at 37 °C. At designated times, the disks were moved to 7 mM EDTA for quenching the enzyme activity and lyophilized once again. This was repeated over many samples, each corresponding to a particular time, to yield the remaining mass (%) or the cumulative mass loss (%) in PBS or in collagenase. For release studies, the hydrogel cocktail was formulated to contain 100 μg/mL of FITC-dextran (40kDa) before being cast into disks (φ=4.5 mm and T=1.6 mm) and UV-crosslinked. The hydrogel disks were placed in 400 μL of 2.5 U/mL collagenase or PBS (both containing 1% Antibiotic Antimycotic) following crosslinking. At designated time points 2 μL of supernatant was sampled and the fluorescence intensity was measured using a Take3® plate and Synergy HT (BioTek) plate reader. To maintain constant enzyme activity, the bathing collagenase solution was replaced with a fresh solution every 2-3 days. The cumulatively released FITC-dextran was then analyzed using relevant mathematical models to provide insight into the influence of chemical composition and water distribution on release.

3.2.5. In-vitro study

The cell culture inserts were plasma treated for 15min in a plasma cleaner (Harrick Plasma, NY). Immediately after treatment, 50μL of warm filter-sterilized 5mol% and 20mol% poly(GelMA-*co*-HEMA-*co*-HPMA) were transferred to the inserts. After a few second, 40μL of the cocktail was taken our leaving 10μL cocktail in the insert which were subsequently crosslinked in UV-crosslinker for 180 sec. The inserts then were exposed to ambient UV in a biosafety cabinet for 1 hour for sterilization. The HUVECs were cultured according to the protocol by Sigma-Aldrich [14]. After confluency, the cells were trypsinized and counted with hemocytometer and diluted to $1x10^5$ Cells/mL. Subsequently, a 200 μL aliquot of cell suspension were transferred to hydrogel coated cell culture inserts or control (coated with 2% gelatin) led to cell density of $6.6x10^4$ Cells/cm^2. Cells were incubated for 4 days, and then fixed with 4% formaldehyde, permeabilized with 0.1% Triton x-100, blocked with 5% BSA and stained with rhodamine-phalloidin and DAPI for visualization.

3.3. Results and Discussions

3.3.1. Hydrogel characterizations

Degree of hydration- According to **Figure 10A**, the DoH of 0.1 and 1.0 mol% poly(GelMA-co-HEMA-*co*-HPMA) were ~82% and are shown to be higher than the DoH reported for poly(HEMA-*co*-HPMA) of 70% [77]. As the concentration of GelMA was increased to 5 mol% and above, the DoH raised to around 90%, a 12% increase, which then dropped sharply to 60% at 87 mol%. The addition of small and increasing amounts of GelMA conferred the high hydration characteristics of this natural polymer to the biohybrid hydrogel. However, at high GelMA content, the high cross linker concentration overshadowed the swelling and resulted in reduced hydration.

Distribution of water- The ratio of W_f/W_{nfb}, known to be a key feature influencing the biotechnical properties of hydrogels, was larger than unity for all compositions showing the higher freezable water content of the hydrogel (**Figure 10B**). The 2.5-fold increase in this ratio in 5 mol% GelMA compared to 1 mol% GelMA followed exactly the fold-increase of water uptake suggesting that the difference of adsorbed water by hydrogels present as freezable water within the hydrogel.

Compressive modulus- The compressive elastic modulus shown in **Figure 10C** demonstrates the ability of polymer to withstand load without deformation. Despite of the importance of total water content within hydrogel on this factor, the ratio of freezable: non-freezable bound water (W_f/W_{nfb}) within the hydrogel which dictates the stiffness of the material[77, 107].

All suggesting that the trend does not follow a simple "rue of mixture" and GelMA likely behaved differently at various concentration.

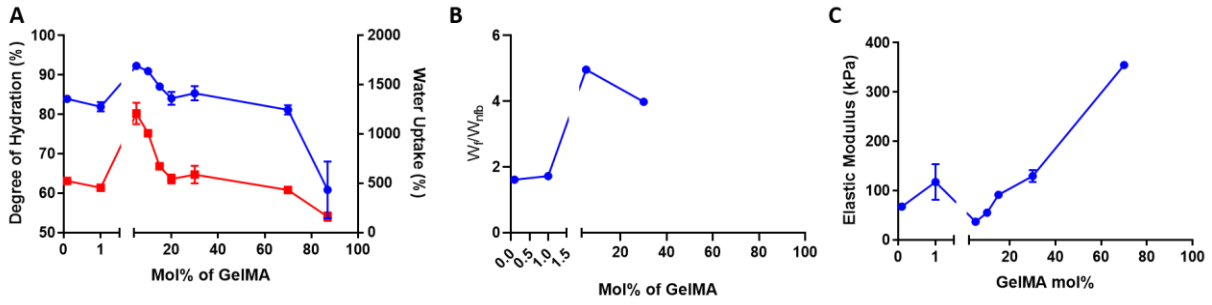

Figure 10. Characterization of poly(GelMA-*co*-HEMA-*co*-HPMA) hydrogels. (A) Degree of hydration, (B) water distribution, and (D) compressive modulus

3.3.2. Degradation profile of hydrogel

The remaining mass of hydrogel of different compositions in the presence of collagenase or PBS was monitored and is shown in **Figure 11**. At 0.1 and 1.0 mol% GelMA the degradation was slow, and the mass loss was at around 40% after 50 days. As the concentration of GelMA was increased, the compositions with 5 to 30 mol% GelMA degraded at a higher rate, being completely degraded

within 6 h and ~10 days, respectively. The trend of mass loss changed again at very high mol% of GelMA. Hydrogels fashioned with 70 and 87 mol% GelMA lost only 29 and 11% of their mass, respectively after 5 days. At very low concentrations of GelMA, 0.1 and 1.0 mol%, which accompanied by 0.5 mol% TEGDA as others, it seemed that the network integrity was held with the low TEGDA crosslinker even after degradation of GelMA. The cleavage of GelMA chains though resulted in marginal loss of mass. For poly(GelMA-*co*-HEMA-*co*-HPMA) hydrogels with higher concentrations of GelMA, the contribution of GelMA in the network was substantial compared to other synthetic substituents, hence its degradation resulted in the whole network to decompose and eventually be dissolved in the bathing solution. At very high GelMA content, as a major part of hydrogel was formed from GelMA, the formulation of the polymer resulted in a highly crosslinked network. Two events likely contributed in the slow degradation of these hydrogel formulations, the highly crosslinked network hindered the free diffusion and movement of enzyme within the network and the amount of enzyme was not enough to catalyze the considerable amount of gelatin in the hydrogel, hence the polymer degraded at an apparent slower rate. This hypothesis is well reflected in the observed physical characteristics of the degradation pattern of hydrogels. Hydrogels with 5-15 mol% GelMA became “mushy” and were very soft in the presence of collagenase as the network lost its integrity showing a bulk degradation pattern. Those hydrogels with higher GelMA content showed more surface degradation with disks that became thinner and smaller in size but maintained their physical integrity until being fully degraded. The 0.1 and 1 mol% had minimal changes of shape during the degradation process.

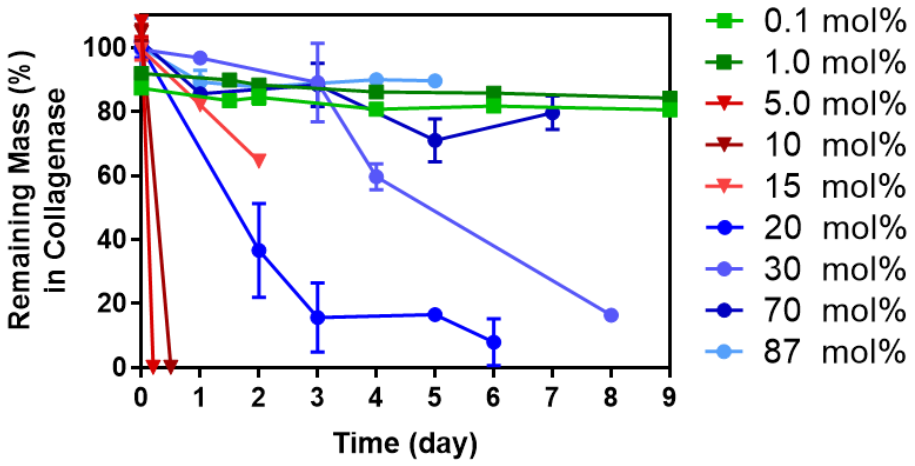

Figure 11. Degradation of poly(GelMA-*co*-HEMA-*co*-HPMA) hydrogels based on remained mass after incubation in collagenase.

The results of degradation profile along with static characteristics (DoH, water distribution, and modulus) of the various formulations outlined a domain-controlled response of hydrogels to GelMA concentration. It suggests that there is a critical point in the balance of synthetic: natural constituents where the role of GelMA changed from acting like a crosslinker to becoming a main component. GelMA is synthesized having ~8 methacrylate groups on each chain. Increasing the GelMA content increase the probability of the chain entanglement and inter- and intra-molecular crosslinking which resulted in a more compact network with smaller void fraction to accommodate swelling and enzyme penetration. GelMA being derived from the hydrolysis of collagen, forms strong intra- and inter-molecular hydrogen bonds with adjacent gelatin molecules resulting in the formation of beta-sheets, a compact robust structure, that does not allow water penetration. These observations allow the grouping of the GelMA hydrogels into three categories: 1) low GelMA content where GelMA ranges between 0.1 and 1 mol%, 2) medium GelMA content where the GelMA concentration ranges between 5-15 mol%, and 3) high GelMA content where the GelMA concentration is more than 20 mol% GelMA.

3.3.3. Release profile of FITC-dextran from hydrogel

The release of FITC-dextran (**Figure 12**) from degrading hydrogels is influenced by cleavage of the degradation sites and diffusion of the payload into the bathing solution or media. The molarity of GelMA in this study falls within a range of 0.05–1 mM, if it is assumed that all GelMA are accessible for the enzyme which is not, as at 50 mol% the hydrogels is highly crosslinked and not likely prone to bulk degradation at least in early time. Abehaki et al. reported a Michaelis constant, K_M, of 0.26 mg/mL for collagenase produced by *Bacillus licheniformis F11.4* on collagen from fish skin K_M was reported to be around 1 mM if the molecular weight of the collagen was about 300 kDa. Hence, the hydrogel degradation, which follows the enzyme kinetics, could be simplified to follow equation. 21. As a result, changes in the average molecular weight of gelatin could be estimated with equation 23.

$$\frac{\overline{M_c}\,(t)}{\overline{M_c}\,(0)} = \exp\left(-\frac{V_{max}}{K_M}\,t\right) \tag{23}$$

The release of FITC-dextran (40kDa) described by Peppas-Sahlin equation presented earlier (equation 14) assumes that diffusivity is constant during the release of the payload. In the case of a degrading polymer, the diffusivity may not be constant and accordingly changes over time as the hydrogel degrades. The time-dependent diffusivity is proportional to the reciprocal of the average molecular changes according to equation 24 [108].

$$D(t) = D_0 \frac{\overline{M_c}\,(0)}{\overline{M_c}\,(t)} = D_0\, exp\left(\frac{V_{max}}{K_M}\,t\right) \tag{24}$$

For the control experiment of FITC-dextran released in PBS, although no enzyme degradation occurs in the absence of enzyme, as this is a study of release from a non-equilibrated hydrogel, the swelling of the hydrogel also affects this release process, especially as data confirmed the hydrogels were highly swellable and adsorbed more that 500% water (**Figure 11A**), the

assumption of constant diffusion coefficient is not valid. A non-constant diffusion coefficient become more important as this model was used in the early phase of release (M_t/M_∞ <0.6) which is more prone to the influence of swelling dynamics. Swelling occurs as the water molecules diffuse into the polymer network which mathematically is similar to the diffusion of FITC-dextran out of the hydrogel. The swelling dynamics similarly follows Fick's second law of diffusion and resulted in a time-dependent diffusivity as given by equation 25 [109, 110].

$$D(t) = D_0 \exp(k\,t) \tag{25}$$

By combining equations 16 and 24 and/or 25, the fractional FITC-dextran released from a degrading poly(GelMA-*co*-HEMA-*co*-HPMA) hydrogels in the presence of collagenase and at early times (M_t/M_∞ <0.6) could be estimated with the model presented in equation 26.

$$\frac{M_t}{M_\infty} = (D_{0,\ Fickian} * exp(k_{Swelling}, \frac{V_{max}}{K_M} t) * t)^{0.5} - D_{0,\ Relaxation} * exp(k_{Swelling}, \frac{V_{max}}{K_M} t) * t \tag{26}$$

By replacing the rate constant with tie constant according to 27, 28, and 29:

$$\tau_F \equiv D_{0,\ Fickian}{}^{-1} \tag{27}$$

$$\tau_R \equiv D_{0,\ Relaxation}{}^{-1} \tag{28}$$

$$\tau_{S,D} \equiv (k_{Swelling}, \frac{V_{max}}{K_M})^{-1} \tag{29}$$

Equation 16 can be re-written as equation 30 which was used to analyze the data:

$$\frac{M_t}{M_\infty} = ({}^1\!/_{\tau_F} * \exp({}^1\!/_{\tau_{S,D}}\, t) * t)^{0.5} - {}^1\!/_{\tau_R} * \exp({}^1\!/_{\tau_{S,D}}\, t) * t \tag{30}$$

The results obtained when using this model for the release of FITC-dextran (40kDa) from poly(GelMA-*co*-HEMA-*co*-HPMA) hydrogels are summarized in **Table 6**.

In all domains, the degradation/swelling time constant inferred from the released FITC-dextran in PBS was smaller in collagenase containing PBS, suggesting the effect of enzymatic degradation in increasing the magnitude of this time constant. The time constant, $\tau_{Swelling,\ Degradation}$ for the hydrogel in enzyme was affected by both swelling and degradation. The three-fold decrease when compared to the condition in PBS, where only swelling occurred, confirmed the mutually reinforcing role of swelling and degradation when the hydrogel was in the presence of the enzyme. While the $\tau_{Swelling,\ Degradation}$ in collagenase was smaller than in PBS in all hydrogels, the fold-decrease was different in various domain being one third in low, one sixth in medium and one tenth in high domains. It suggests that degradation affects the release of FITC-dextran 40kDa from hydrogels with low swellability and more non-freezable water and degradation. The low swellability of hydrogel indicates a smaller void fraction and pore size in hydrogel, therefore the loaded dextran was less able to get out of the hydrogel through diffusion. The surface degradation of the gel or swelling caused the dextran to be released from highly crosslinked hydrogel network in high domain. When three time constants were compared within each hydrogel composition when in collagenase, the swelling/degradation time constant was smaller among the three, suggesting the significant role of swelling/ degradation in the release.

While all loaded with equal concentrations, the cumulative FITC-dextran that was released from the hydrogels was different based on the hydrogel composition. A FITC-dextran final concertation of 10 μg/mL was recorded for 15 mol% GelMA in collagenase which was reduced to 7.5 and 4.6 μg/mL from 0.1 and 1.0 mol% GelMA, 7.2 and 3.3 μg/mL from 20 and 87 mol% GelMA, respectively. The higher release from 15 mol% GelMA was in accordance with the faster degradation of this hydrogel formulation.

Using approaches different molecule weights of FITC-Dextran in release studies and changing the degree of methacrylation of the GelMA while keeping the composition constant would likely give a better insight into the balance between degradation and swelling in affecting the release of drug conjugate.

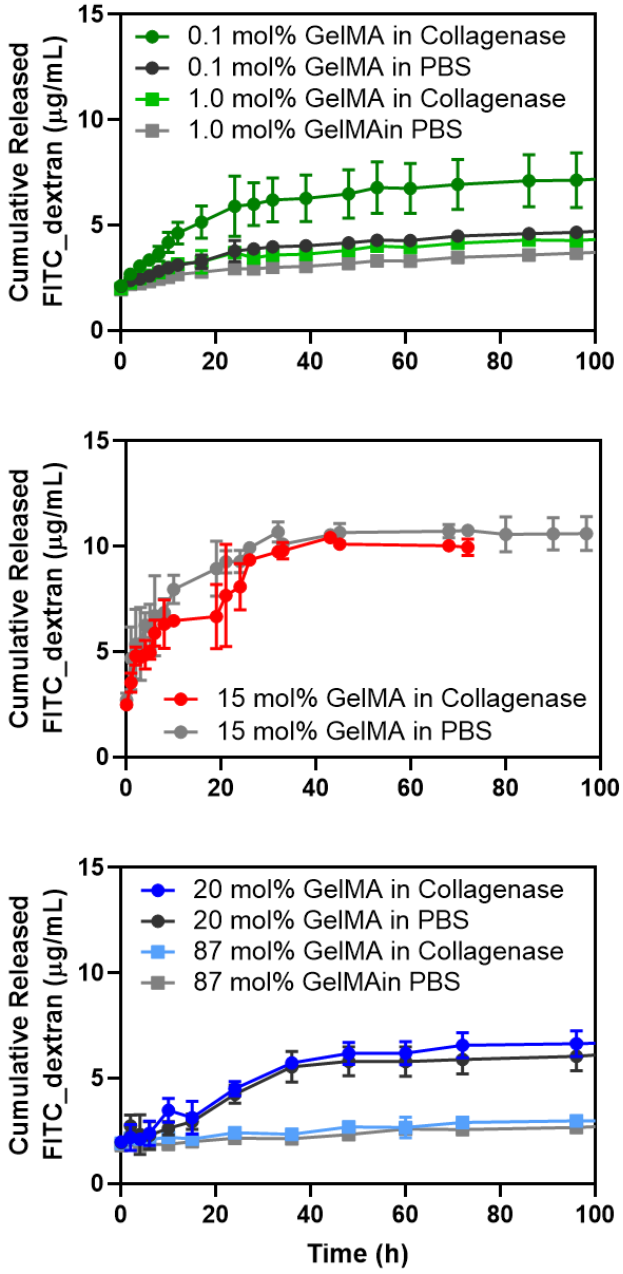

Figure 12. The Release of 100 µg/ml FITC-dextran 40kDa payload from poly(GelMA-*co*-HEMA-*co*-HPMA) hydrogels at (A) low, (B) medium, and (C) High GelMA content in 2.5 U/mL collagenase type 2 and PBS.

Table 6. The kinetic of total FITC-dextran released from poly(GelMA-co-HEMA-co-HPMA) hydrogels in 2.5 U/mL collagenase and PBS.

	0.1mol% Collagenase	0.1mol% PBS	1.0mol% Collagenase	1.0mol% PBS	15mol% Collagenase	15mol% PBS	20mol% Collagenase	20mol% PBS	87mol% Collagenase	87mol% PBS
$\tau_{Fickian}$ (h)	293	109	247	125	32	14	929	516	363	182
$\tau_{Relaxation}$ (h)	668	267	594	287	79	33	2206	4223	∞	453
$\tau_{Swelling, Degradation}$ (h)	5	15	11	39	13	77	8	81	18	158

3.3.4. *In-vitro* study

The florescent images of cells grown on hydrogels coated inserts are shown in **Figure 13**. On hydrogel coated inserts **Figure 13A** and **B**, the cell attachment followed the path of hydrogel presence. The results showed that the hydrogel is supportive of cell attachment and growth. The density of cells was higher on 20 mol% GelMA hydrogels compared to 5 mol% as it provided more attachment motifs for cells. The cells spread relatively more uniformly on the control gelatin-coated insert as shown in **Figure 13C**.

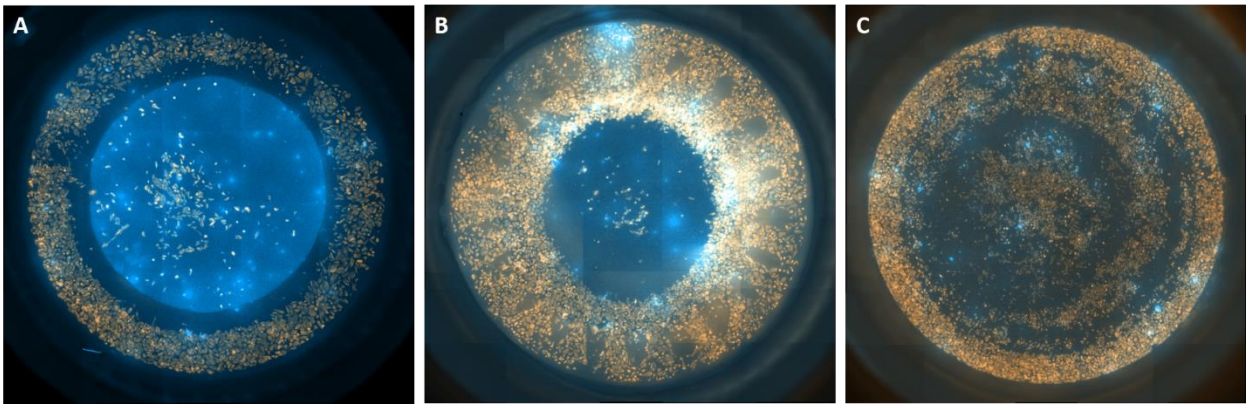

Figure 13. Growth of HUVECs on cell culture insert coated with (A) 5 mol% and (B) 20 mol% GelMA in poly(GelMA-*co*-HEMA-*co*-HPMA), and (C) gelatin coated.

3.4. Conclusions

Three unique domains of GelMA concentration have been identified in the performance of biohybrid poly(GelMA-*co*-HEMA-co-HPMA) hydrogels. Based on both static and kinetic characterization these domains of low (0.1-1.0), medium (5-15) and high (>20) suggest the GelMA mol% content may be used as a tool to control: 1) degradation, 2) release of payload, and 3) favorable cell-scaffold interactions. Collagenase activity served to increase the release of the factor surrogate but did not alter the mechanism of release for which the rate-controlling step remained diffusion and not enzyme kinetics. The use of a 20 mol% GelMA containing poly(GelMA-*co*-HEMA-*co*-HPMA) hydrogel is indicated for its balance of uniform surface degradation, well controlled release of factor surrogate, and favorable density of motifs for the recruitment and attachment of HUVECs. Paracrine release of growth factor should be independently studied, as protease degradation will likely also influence factor activity. The characterizations performed in this study have established the baseline of performance needed to choose the right GelMA content of a biohybrid hydrogel when engineering a bioactive scaffold for the recruitment of HUVECs and the simultaneous degradation-associated release of factors to those cells when used as a scaffold.

4. ELECTRIC CELL STIMULATION OF HUVECS GROWN IN 3-D CULTURE[3]

4.1.Introduction

Potentiation of cellular behavior under the influence of mild, sustained and discerning electric fields (EFs) has been a noble cause of much research [18, 111, 112]. The need for improved understanding of the physiological response of living cells grown in culture under the influence of such fields necessitates development of systems for the simultaneous application of EFs and recording of cellular responses. The nascent production of electroceuticals, locally produced changes in biochemical activities or biomolecular fluxes under the influence of an EF is an example of the efficiency of harnessing electrical impulses to treat ailments [113]. The effective roles of passive electrical cues [13] and external endogenous electrical fields (EF) *in-vivo* prompted the use of electrical stimulation (ES) *in-vitro*, both to better understand the molecular pathways through which EFs affect cellular process as well as applying such cues as a tool to control and guide cellular response, e.g. differentiation [111]. This premise has been addressed by developing devices, systems and setups for electrical stimulation (ES), of *in-vivo* range, in a controlled manner to the cells in culture, *in-vitro*. The application of ES has been associated with concomitant heat generation, local pH disruption, accumulation of chemical components (polarization) and possible chemical reactions in the media [114-116]. Electrification systems have been developed over the years to address the forgoing named issues as well as personalize the system for specific application [117-119]. Providing a means to deliver electrical signals *in-vivo*

[3] Excerpted and reprinted with permission from "Design, fabrication and testing of an electrical cell stimulation and recording apparatus (ECSARA) for cells in electroculture" by Abasi, Sara, Aggas, J.R., Venkatesh, N., Vallavanatt, I.G., Guiseppi-Elie, A., 2020. Biosensors and Bioelectronics, 147, 111793, Copyright [2020] by Elsevier. https://doi.org/10.1016/j.bios.2019.111793

is beneficial in other areas including development of electrocuring bioadhesives where electric potential is used to initiate the crosslinking of monomers [120, 121].

One of the early approaches to apply an EF was to use Ag/AgCl electrodes through agar salt bridges. This approach used reversible, separated electrodes such that the inherently harmful bi-products of electrification (e.g. reactive oxygen species, free silver ions, or wild shifts in local pH) were made as far away from the living cells as possible [122]. More recently, Xiong et al. developed an agar salt bridge cell stimulation platform capable of applying DC and square waves at multiple frequencies in a 6-well system [118]. While effective, there are some inherent limitations including possibility of contamination, limitation of stimulating signals, duration of the applied field and recording of an impedimetric response were not addressed. Vunjak-Novakonic's group developed a system consisting of two parallel carbon electrodes in a 6 mm petri dish for stimulating cells within a 3-D construct [117]. Carbon was selected over traditional metals such as platinum or gold as it showed the highest charge transfer resistance in biological studies [123]. In this setup, the two rod electrodes were placed on either side of the cell growing plane. The uniformity of EF between the two electrodes and the field strength delivered to the cells are questionable and dependent on the shape and size of electrodes as wells as the scaffold where the cells were cultured. Mobini et al. reported the development of a system which is a simple practical modification of a common 6-well cell culture plate which provides a means of running multiple samples under analogous conditions, again, the electrode placement was similar to the previously developed carbon electrode system, rendering EF uniformity questionable [119]. Other suggested and developed setups are mostly based on similar electrode configurations. Among these are the 2.5 cm separated coplanar pair of carbon electrodes to deliver DC and pulse signals to HUVEC cells [124], the Independently Addressable Interdigitated Microsensor Electrodes (IAIMEs)

fashioned from gold (IAIME Au), platinum (IAIME Pt) or indium tin oxide (IAIME ITO) of ABTECH Scientific Inc., a similarly configured coplanar arrangement of 5, 10, 15 or 20 μm line and spaced electrodes for the study of cell mobility and migration via electrical impedance [125], the Biomet® OrthoPak® Non-invasive Bone Growth Stimulator to improve bone healing rates [126], and C-DISH^{TM} launched by IONOPTIX to apply pulse electric fields to cardiomyocytes [127]. Despite promising results from a wide range of electrode configurations and patterns of stimulation, the field of electrified cell stimulation still lacks a single system for doing multiple simultaneous experiments using various stimulation wave forms with simultaneous interrogation.

Another entirely different approach in electrophysiology is to use the electrical properties of cells as a real-time tool for monitoring cellular processes pioneered by Giaever and Keese in 1984 [128]. Impedance, the opposition that a system presents to a current when a voltage is applied, has been employed as a meaningful parameter to describe cellular response. Electrical impedance spectroscopy (EIS), the application of a spectrum of interrogating voltage frequencies, is a powerful though non-specific tool that is widely used to study the performance of neural electrodes [129], organoid bodies in organ-on-a-chip models [130], and in drug screening [131]. The power of the EIS technique is found in the application of the principles of electrodics to the dynamics of cellular behavior (cell mobility, tight junction formation, ion channel activity, etc.) and sub-cellular components (membrane permeability, inclusion bodies, polarity of the cells, directional alignment, etc.) that appear in the resultant complex impedance. EIS data can be analyzed with equivalent circuit models as simple as the Randles model or more complex models to continuously study cellular behavior[132]. Lo and Ferrier applied mathematical equations to the experimental data to model the flow of electrical current into and between the cells seeded on ECIS (Electric Cell-substrate Impedance Sensing), the biosensor developed by Giaever and Keese, which was

later commercialized by Applied Biophysics [133, 134]. Another commercially available system is the impedance-based real-time cell analyzer (RTCA) system by ACEA Biosciences. This system uses transmission line impedance to monitor changes in cellular impedance behavior [135]. The cellZscope launched by nanoAnalytics is specialized for measuring the transepithelial/- endothelial impedance/ resistance of the cells (TEER) [136]. A pair of stainless-steel parallel electrodes were used to measure the impedance of the cell layer formed on a cell culture insert. Applied BioPhyisics subsequently offered a very similar device for TEER measurement called TEER 24.

In this chapter, a dual-function Electrical Cell Stimulation and Recording Apparatus (ECSARA) was designed, fabricated, programmed and applied with the aim of addressing deficiencies of currently available systems while demonstrating improved performance and reliability. Furthermore, while the available systems were developed to perform either as a bioreactor or a monitoring device, the current system of this study combines the two paradigms to allow concomitant electrical stimulation using variable wave forms and duty cycles in bioreactor mode while periodically and systematically in a fully programmed manner, measuring the complex impedance of the cells or organoids under examination. Thus, ECSARA is a tool to apply ES to cells in 3D culture on porous inserts as well as 3-D organoids while monitoring the cellular behavior through their electrical impedance [14].

4.2. Electrical Cell Stimulation and Recording Apparatus (ECSARA)

4.2.1. Design criteria

Applying an electric potential between two infinitely wide ideal electrodes within a vacuum induces a collimated uniform EF between them with a field strength of E= V/d, where *E*, *V*, and *d* stands for EF strength (V/m), applied voltage (V) to the electrodes, and distance (m) between the two electrodes, respectively. The forgoing establishes a uniform gradient between the idealized

electrodes. For real electrodes subtending real cell culture media, the distribution of the electrical field is not uniform, and the gradient is not linear. The ECSARA seeks to apply a uniform EF to all cells with an expectation that all cells experience the same EF. This was achieved by placing two opposing disk electrodes with their disk faces parallel to each other and on either side of the plane of cell culture. This electrode configuration ensures that all the cells in culture were exposed to a uniform, consistent field. The strength of the effective electric field (E) between the electrodes is governed by Gauss' law: $E=\sigma/(k\varepsilon_0)$, where σ is the sheet charge density (C/m^2), *k* is the dielectric constant, and ε_0 is the permittivity in vacuum (8.85×10^{-12} F/m). With the promise of keeping the cells away from direct contact with electrodes, hanging cell culture inserts were used to suspend the cells equidistantly between the two electrodes. These inserts provide a specific footprint for cell culture to accommodate either direct cell seeding or as a substrate for scaffolds/tissues/organoids between the electrodes as well as enabling simple transfer of cultures from the ECSARA for imaging or other evaluation purposes. There exist multiple options for insert footprint (e.g. ϕ=0.65 cm or A=0.3 cm^2), pore size (0.4 - 4.0 µm) and membrane material (polyethylene terephthalate, polytetrafluoroethylene, mixed cellulose esters or polycarbonate). In order to accommodate the standard commercial insert, the ECSARA electroculture plate was fashioned as the same physical design parameters as a standard 24-well cell culture plate.

4.2.2. System configuration

The ECSARA system comprised the following four main components: i) the 24-well electroculture plate (base, body, and lid), ii) the interrogation hardware of signal generator, frequency response analyzer, multiplexer unit, computer, and associated cabling, iii) the controlling and data acquisition software, and iv) the data processing and analysis software.

4.2.3. The 24-well ECSARA electroculture plate

The 24-well ECSARA electroculture plate is a modular design, made of a three-part polymeric chamber outfitted with metal electrodes. The chamber consists of three discrete parts: lid, body, and base, all produced from an FDA approved polypropylene (EP42HT-2Med, Tecapro MT, Total Plastics, Fort Wayne, IN). The Tecapro MT meets the USP Class Vl requirement which addresses the in-vivo cytotoxicity of the material extracts. The chamber was fabricated from a design developed in Solid Works 2018 (Dassult Systems) using CNC machining (Haas Mill G Codes) with an accuracy of 0.0001" (inches). Early designs were produced, inspected and validated by rapid prototyping using a desktop 3-D printer (Stratasys Mojo). All critical external and internal dimensions of the chamber were selected to replicate a common 24-well tissue culture plate. Figure 14A is an exploded view that shows individual parts and final assembly of the actual electroculture plate. Titanium grade 23 (6AL-4V ELI) (TMS Titanium, Poway, CA) was used for electrodes of each well. The top electrode was sourced as rod stock and cut into discrete lengths and the bottom electrode sourced as sheet stock and cut into plates. Titanium Grade 23 is an alloy that consists of titanium (88.5 - 91 % purity), carbon (0.08 % max), nitrogen (0.03 % max), oxygen (0.13 % max), hydrogen (0.0125 % max), vanadium (3.5-4.5 %), aluminum (5.5-6.5 %), and iron (0.25 % max). The electrode system comprised a single rectangular plate (127 x 85 x 33 mm) that served as a common return electrode beneath all 24 wells and 24 opposing, independently addressable rod electrodes (ϕ = 4.78 mm and L = 12.44 mm), each rod corresponded to a single well. The sheet and rod electrodes were mounted within the base and lid, respectively, which kept them separated by 7.4 mm when in place. The independent wells were sealed with medical grade Viton O-rings (Apple Rubber, Lancaster, NY) that were placed beneath each well within a circular groove devised for it which limited the area of the bottom electrode to a disk of 9.91 mm diameter. The

rod electrodes were sealed into hollow cylindrical housings that extended downwards from the lid using a cytocompatible, two-component epoxy (EP42HT-2MED clear, MASTER BOND, Hackensack, NJ). The epoxy formed a thin layer around the metallic rods to both secure them into the cylindrical housings and ensure that no fluid could seep between the rod and its housing. Thus, a two-electrode electrification system comprised of A_1 = 17.95 mm^2 (top electrode), A_2 = 77.08 mm^2 (bottom electrode) separated by 7.4 mm was fashioned. The base and body were screwed together with twelve Type 316 stainless steel bolts and nuts, evenly distributed throughout the plate to provide a uniform pressure to the O-rings and thus seal the wells. Electrical connections were provided by a 25-lead flat cable (28G) secured to each of the 24 rods, through a stainless-steel screw (Super-Corrosion-Resistant, 2-56 Thread Size, 1/8" Long) into the head of the rod. The 25^{th} lead served the return electrode.

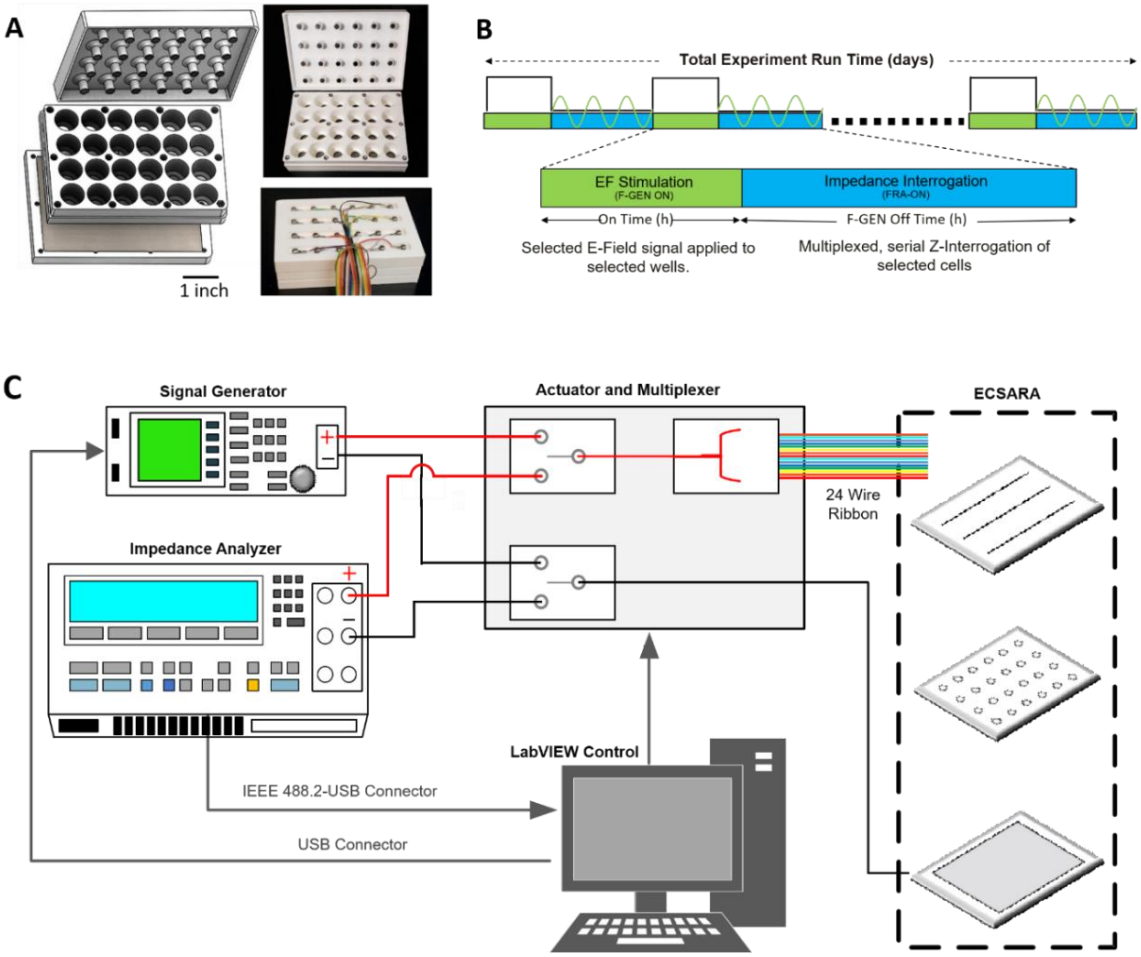

Figure 14. (A) An exploded schematic and photographs of the ECSARA electroculture plate showing lid, body, and base of the electroculture plate with the photograph of the assembled but opened plate showing top and base electrodes and electrical connections to the top and bottom electrodes. (B) The timeline of the electric field stimulation and impedance interrogation commands used by the software, and (C) Schematic illustration of ECSARA showing the instrumentation control and data acquisition system (hardware).

4.2.4. Interrogation hardware

The interrogation hardware comprised of a signal generator (SDG1025, Siglent, Solon, OH) to deliver electrical cell stimulation, a frequency response analyzer (FRA) (Solartron 1260A, Ametek Inc., Berwyn, PA) to collect EIS data, and a data acquisition/multiplexer unit (34970A, Hewlett Packard, Palo Alto, CA) to multiplex the signal between the generator and FRA as well as sequentially among each individual well of the 24-well electroculture plate. The interrogation

hardware was designed so that at any given time, either the signal generator or FRA could be turned on and into use. As shown in Figure 14C, both working electrodes of the signal generator and FRA were wired to an actuator channel within the multiplexer unit. The output of this actuator was directed to a 24-plex multiplexer, where each output of the multiplexer was directed to one of the 24 rod electrodes located in the cover of the electroculture plate. In a similar fashion, the counter electrodes of both systems were wired to an actuator which was directed to the return sheet electrode. This arrangement allowed the actuators to switch between the signal generator and FRA per need and as programmed. When the signal generator was in use, all 24 channels of the multiplexer were activated, so that an electrical signal could be applied between each of the 24 rod electrodes and the return sheet electrode. When the FRA was in use, each channel of the multiplexer could be sequentially cycled through, allowing for measurement spectra of each individual well.

4.2.5. Controlling and data acquisition software (CDAS)

Custom instrument control and data acquisition software was developed in LabVIEW. The interrogation hardware (signal generator, multiplexer unit, and FRA) communicated via a custom LabVIEW block diagram and Graphical User Interface (GUI) (Figure 14C). The software was written to execute multiple tasks on a loop over a total experiment runtime (usually several days). A timeline of the commands used by the software is shown in Figure 14B. Briefly, an electric signal is applied to selected wells of the electroculture plate for a specified time, then upon completion, the signal generator is turned off, the software triggers the multiplex unit to switch over to the impedance analyzer where impedance spectra are measured in a well-by-well manner. The acquired data are exported into excel workbooks and individual ".z" impedance files.

The GUI was created to allow customized experiments, with variability in which (if not all) of the 24 wells would be used in a particular experiment, including parameters of the simulation signal produced by the signal generator, parameters of the impedance analysis, and the total experiment time. Particularly, the type of signal (square, sinusoidal, triangular, DC), frequency (1 mHz - 50 MHz), amplitude (1 - 20 mV p-to-p) and duty cycle (0-100%) were all programmable. In addition, parameters of the impedance measurements, such as interrogation signal amplitude, frequency window (10 µHz - 32 MHz with 0.015 ppm resolution), and number of points to measure per decade were made variable. The FRA can elecit impedance at frequencies as low as 10 µHz, however, it should be noted that sampling at low frequencies would be at the cost of losing contributions from fast-occurring events. Consequently, the frequency range for impedance acquisition should be set dependent on the type of important information meant to be captured.

4.2.6. Data Processing

The large volume of recorded data (e.g. up to 30 spectral files per well) over the time course of a five-day electroculture exercise) places unique demands on the data processing component of the system. The data captured in excel workbooks and as individual ".z" impedance files were exported and subjected to equivalent circuit analysis using the Expanded Zfit Matlab script. The customized Expanded Zfit Matlab script was used for large scale equivalent circuit analysis and was modified to take the recorded data as input and then output the best values of the electrical circuit elements based on "goodness of fit" (χ^2) criteria applied to several candidate models. To be useful, equivalent circuit analysis must be based on models that have a basis in the physical electrochemistry, electrodics and ionics of the system under examination. Data processing seeks to extract the equivalent circuit elements attributable to the electrochemical and mass transport processes to find the key model parameter representing the device under test (DUT) [137]. Data

processing seeks to extract and ascribe a final membrane resistance (R_{Cell}) and membrane capacitance (Q_{Cell}) attributable to the layer of cells cultured on the cell culture insert between the electrodes. Real-time, temporal complex impedance data acquired in the CDAS module above must therefore be modeled using equivalent circuit modeling and the key model parameter representing R_{Cell} and Q_{Cell} extracted and presented as the desired result.

4.3.Materials and Methods

4.3.1. Materials

HEPES buffer, PBS buffer, potassium ferrocyanide/potassium ferricyanide [Fe(II)/Fe(III)], Dulbecco's Modified Eagle's Medium (DMEM, high glucose), RPMI-1640 Medium (With L-glutamine and sodium bicarbonate) were obtained from Sigma Aldrich. De-ionized, ultrapure water was collected from a Milli-Q® plus (Millipore Inc.) ultrapure water system. For cell culture studies, primary Human Umbilical Vein Endothelial Cells (HUVECs, neonatal pooled, 200P-05N) were obtained from Sigma-Aldrich and cultured according to the protocol provided by the supplier in Endothelial Cell Growth Medium supplied with 1% Penicillin-Streptomycin (10,000 units penicillin and 10 mg streptomycin/mL, PS) (Sigma-Aldrich). Trypsin-EDTA (0.25% trypsin, 0.02% EDTA) solution, trypsin inhibitor and gelatin were similarly purchased from Sigma. Phosphate-buffered saline (PBS) tablets (Gibco, Thermo Fisher Scientific, Waltham, MA) were dissolved in DI water to prepare 0.01 M (pH 7.4) buffer solution. AlamarBlue™ Cell Viability Reagent, rhodamine-phalloidin and DAPI were purchased from Thermo Fisher Scientific. Anti-VE cadherin antibody conjugated to Alexa Fluor 488® was purchased from Santa Cruz Biotechnology (TX).

4.3.2. Temporal impedimetric behavior and well-to-well variability

To evaluate the temporal behavior of the system as well as variability between the wells, the impedance of 2.0 mL of 0.01 M PBS was measured every 6 h over 5 days at 37°C in an incubator (VWR 2310 CO_2 Incubator). Impedance measurements were completed using a 20 mV p-p sinusoidal voltage from 10 mHz - 1 MHz. Prior to impedance measurements, the top rod electrodes were mechanically polished with standard polishing kit using 15.0 µm diamond slurry (5 min) followed by 0.05 µm alumina (3 min) (Bioanalytical System, Inc., IN) then thoroughly rinsed in DI water.

4.3.3. Impedimetric behavior of ECSARA using six physiological media

The impedance of 6 different media: DI water, 0.01 M PBS, 0.1 M HEPES, 0.1 M Fe(II)/ Fe(III), DMEM, and RPMI were separately evaluated. These media were chosen as they are the most common media used in *in-vitro* cell culture studies. The Fe(II)/Fe(III) system is an electroactive couple often used as a redox probe in biosensor studies. Four wells of the 24-well ECSARA were filled with 2.0 mL of each media and impedance spectra were collected in an incubator at 37°C using 20 mV p-p sinusoidal voltage over the range 10 mHz - 1 MHz.

4.3.4. Contribution of cell-culture insert to impedance

To study the contribution of the cell culture insert to the overall impedance of the electroculture well, 12 polyethylene terephthalate (PET) inserts with pore size of 3.0 µm and pore density of 2 x 10^6 pores/cm^2 (Corning, Millipore, MA) were pre-hydrated in 0.01 M PBS and placed within 12 wells of the ECSARA and all the 24 wells were filled with 0.01 M PBS. Impedance measurements were taken under similar conditions as previous tests in the incubator at 37°C every 6 h for 2 days.

4.3.5. Equivalent circuit analysis

Two equivalent circuit models were used to analyze impedance spectra, the simpler of these, the Randles Equivalent Circuit (R(QR)), comprises a solution/membrane resistance (R_S or R_M) in series with a parallel combination of a charge transfer resistance (R_{CT}) and double layer capacitance (Q_{DL}), thus, ($R_{S/M}(Q_{DL}R_{CT})$) [138] [139]. A more complex equivalent circuit was developed to better characterize the system in question ($R_S(Q_{OX}R_{OX})(Q_{DL}R_{CT})$) or ($LR_S(Q_{OX}R_{OX})(Q_{DL}R_{CT})$), in which an additional parallel resistance and capacitance is placed in series after the charge transfer resistance and double layer capacitance to signify the resistance and capacitance of the native oxide layer formed on the surface of the titanium alloy electrodes used (R_{OX}, Q_{OX}). The inductance (L) represents the inherent inductive effect of the ribbon cable which was calculated to be on the range ~2 μH for the diameter (28G) and length (100 cm) of the cable used for connecting the plate to the measuring device. All circuits were used in analysis to extract either the R_S or R_M. The more complex circuit was used as a model to validate the use of the simpler, less computationally demanding Randles circuit. Equivalent circuit analysis was completed using either ZSimpWin 3.60 (Princeton Applied Research, Oak Ridge, TN) or the customized Expanded Zfit MATLAB script (originally written by Dr. Jean-Luc Dellis) [140].

4.3.6. Simulation of electric field (EF) distribution within the well

The 3D geometric model was developed in SolidWorks (2018) according to actual dimensions and placement of the electrodes and cell culture insert (Millicell® Hanging Cell Culture Inserts, Millipore, MA). An electrical field and potential simulation were then carried out using 3D-Maxswell in ANSYS as an electrostatic study. The electrostatic analysis assumes the system to be in the low-frequency electromagnetic domain where the displacement currents are negligible and hence neglected. The analysis is based on the assumption that no current exists in any material and

objects are either perfect conductors with infinite electric conductivity or perfect insulators with zero electric conductivity, respectively. Electrical properties of each material were assigned according to **Table 7**.

Table 7. Electrical properties of the material components used in the simulation of the electric field.

	Conductivity (S/m)	Relative Permittivity
Titanium	1.82×10^{6}	1
Polyethylene terephthalate (PET)	1×10^{-15}	3
Polystyrene	1×10^{-16}	2.6
Phosphate buffer saline (PBS)	1	80

4.3.7. Implementation of ECSARA in real-time monitoring the effect of electric field on HUVECs

To explore the effect of EF on HUVECs, cells were divided into two groups, EF-stimulated cells and non-EF-stimulated cells or control. The temporal impedance response, metabolic activity via Alamar Blue assay, and cell morphology via fixation and staining were examined. Cell culture inserts of pore size corresponding to 0.4 μm and pore density of 1×10^{8} pores/cm^2 (12.6% porosity) (Corning, Millipore, MA) were used to culture HUVECs. The inserts were incubated (30 min) with 50 μL of 2wt% gelatin in PBS and washed three time with PBS prior to cell seeding. HUVECs were cultured to confluency in regular T75 cell culture flask, trypsinized and transferred to inserts at a seeding level of 5×10^{4} cells/mL (3.3×10^{4} cells/cm^2). The viability of cells was determined to be 94% using trypan-blue and hemocytometer prior to seeding. At 6 h post seeding, a pulse of 1.2 V corresponded to electric field of 162 mV/mm at frequency of 1.2 Hz and pulse width of 2 ms was applied to the cells continuously except for the time interrupted for impedance measurement

(approximately 45 min every 6 hours). Same identical cells were used as control with no exposure to the EF. The impedance of the test and control wells was measured every 6 h at interrogation voltage of 20 mV p-t-p and within frequency range of 0.01Hz -1 MHz. The Alamar Blue assay was performed according to standard protocols. Every 24 h, the media of EF stimulated, and control wells was replaced with media containing 10% Alamar Blue followed by 2 h incubation in the incubator. The absorbance of the media was subsequently measured using a Synergy HT (BioTek Instruments, Inc.). the media containing alarm blue was replaced with regular media after running the assay. For visualization, the cells on an insert were fixed (4% formaldehyde), permeabilizated (0.1% Triton x-100), blocked (10% BSA), and stained with anti-VE cadherin antibody conjugated to Alexa Flor 488®, rhodamine-phalloidin, and DAPI. The membrane was then cut away from the insert and the cells were imaged with an inverted Zeiss fluorescent microscope (Observer Z1).

The EIS data collected prior to seeding (media with insert) were modeled to $R_M(Q_{OX}R_{OX})(Q_{DL}R_{CT})$ to extract the values of those equivalent circuit elements which remain constant in the system. The data collected from continuous EIS measurement following cell seeding were subsequently fitted to $LR_M(Q_{Cell}R_{Cell})(Q_{OX}R_{OX})(Q_{DL}R_{CT})$ keeping the values of L, Q_{DL}, and R_{CT} constant from the fitted model on the data without cells. Q_{Cell} represents the capacitance that the cellular layer introduced to the system due to their charged membrane and R_{Cell} represent the trans-cellular resistance due to tight junction formation between the cells as they form a confluent monolayer and establish a transmembrane resistance.

4.3.8. Statistical analysis

Outliers, which were defined as values outside the 1.5 interquartile range (IQR) of first and third quartiles were removed. Blocking of data in a randomized complete block design (RCBD) was

performed using JMP 13.0 (SAS group) for more meaningful comparison. The means were compared together using a student t-test and p-values < 0.05 were considered significant.

4.4. Results and Discussion

4.4.1. Temporal study and well-to-well variability

Impedance spectra of cells in culture supported on inserts that were measured continually over a six-day period were expected to reveal changes in their trans-membrane permeability, the quality of tight-junctions between and among cells and the overall density of cells. These were expected to manifest as changes to the value of the cell-related circuit elements of an appropriate equivalent circuit model. However, changes in the media pH, redox potential (EH), ion concentration, protein production and protein adsorption onto electrodes are expected to contribute to temporal changes in impedance spectra. These must be distinguished from temporal drift arising from changes to the system itself. System drift was measured as a temporal effect to the resolved solution resistance, R_S, of 0.01 M phosphate buffered saline (PBS) determined every 6 h over 5 days at 37°C. R_S was calculated by modeling the EIS data using an $R_S(Q_{OX}R_{OX})(Q_{DL}R_{CT})$ model. A randomized complete block design (RCBD) was used by taking the response of the 24 wells as a block. Other than four time points where R_S was significantly different ($p < 0.01$), the magnitude of R_S remained the same over the entire time period. Well-to-well variability was studied from the temporal analysis of R_S, which showed no discernable pattern with time. To evaluate the variation between the wells, R_S for each well was averaged over time. The average of each well was then compared with other wells using RCBD and taking the time as a block. The average R_S of the wells was $37.59 \pm 5.29\ \Omega \cdot cm^2$ with one well that was significantly different ($p < 0.01$) from the rest.

Figure 15A shows the elements of the R(QR)(QR) equivalent circuit averaged over 24 wells measured at five time points (every 24 h) when the wells contained PBS at 37°C. **Figure 15B** shows the magnitude of R_S for four randomly selected wells as well as the average of all 24 wells over time. Statistical analysis showed that R_S did not depend on time and the variation did not follow a time-based trend. R_S, solution resistance, was chosen to represent stability of the system as all the events occurring within the solution in this case are counted in this parameter. The pattern of variation suggests that the R_S values extracted from impedance measurements might have been sensitive to some other factor, possibly some environmental factor such as vibration of the work platform and/or electrical noise in the room.

The possibility of using the simpler $R_S(Q_{DL}R_{CT})$ model was evaluated. The χ^2 for $R_S(Q_{DL}R_{CT})$ and $R_S(Q_{ox}R_{ox})$ $(Q_{DL}R_{CT})$ was 0.60 ± 0.09 and 0.50 ± 0.08, respectively. The results showed that the magnitude of R_S (a parameter of interest) was at maximum 2% different from the values calculated from $R_S(Q_{ox}R_{ox})(Q_{DL}R_{CT})$ and followed the same trend (data not shown). The variation of R_S however was slightly higher for $R_S(Q_{DL}R_{CT})$ compared to the $R_S(Q_{ox}R_{ox})(Q_{DL}R_{CT})$ model, therefore the more complex R(QR)(QR) model was found to be more appropriate for data interpretation.

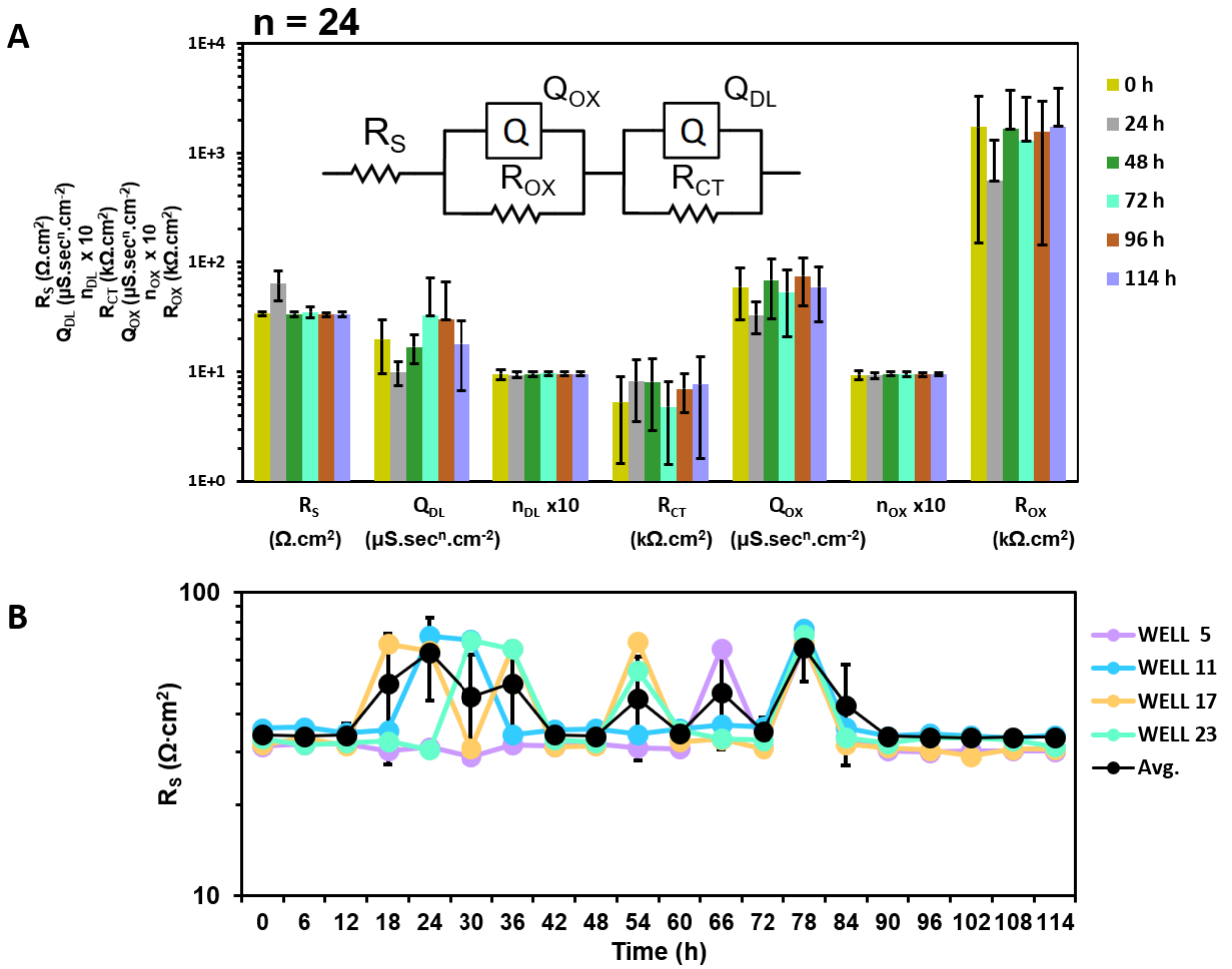

Figure 15. Results of the temporal and well-to-well variability study showing (A) the result of equivalent circuit analysis of EIS data collected from 0.01 M PBS every 24 h averaged over 24 wells and (B) the changes in magnitude of Rs over 5 days shown for four randomly selected wells and the average of all 24 wells.

The titanium alloy used in the system is a commonly used material in biomedical implants, because of the formation of a biocompatible and corrosion resistant passive oxide layer (principally TiO_2) [141]. One of the design concerns was that the formation of such an oxide layer would change the temporal electrode characteristics hence affect the impedance. The result of the temporal study indicated that such chemical phenomena did not contribute in the magnitude of solution or membrane resistance in the configuration employed. It was shown by Tamilselvi et al., however, that formation of an oxide layer on Ti–6Al–4V ELI alloy changed the charge transfer resistance and double layer capacitance significantly. In the same study, the formation of a stable passive

oxide layer was estimated to occur during 360 h. It should be noted that the cleaning technique that was applied in the mentioned study [141] was more aggressive than what was used for ECSARA. In fact, a gentler polishing, that is good enough to clean the electrodes but not completely remove the oxide layer, was preferred in this study in order to have a stable electrode performance. While the presence of an oxide layer increases the charge transfer resistance, there is not a practical way to prevent growth of such a native layer hence the electrodes won't be stable in the case of complete removal. Moreover, the formation of the oxide layer results in the current being delivered capacitively which is a safer way to deliver electrical stimulation to the living specimens. It is for the forgoing reasons that cells were presented in a stand-off configuration on cell culture inserts and not in direct contact with electrodes.

4.4.2. Characterization of the ECSARA with different media

The difference in the electrolyte strength of the media considerably affected the magnitude of the double layer capacitance, Q_{DL}, and charge transfer resistance, R_{CT}, but was expected to principally affect the magnitude of the solution resistance, R_S. Therefore, to more accurately identify the magnitudes of Q_{DL}, R_{CT}, and R_S, the inductance (L) element, representing the system's cabling, was added to the equivalent circuit model. The results of equivalent circuit LR(QR)(QR) model analysis is summarized in **Figure 16**. The magnitude of inductance was calculated to be 9 ± 2 $\mu H \cdot cm^{-2}$ for different media which was a very close approximation to what theoretically calculated for the specific ribbon cable used in this system. The size of Q_{DL} was calculated to be ~0.5 $nS \cdot sec^{n} \cdot cm^{2}$ for DI water and HEPES (weak electrolyte) and ~20 $\mu S \cdot sec^{n} \cdot cm^{-2}$ for PBS, DMEM, RPMI, and Fe(II)Fe(III) (redox electrolyte). Higher ion content in the later groups resulted to larger double layer capacitance [142]. The capacitance and resistance attributed to the oxide-laden interface were retained in the range of ~12 $\mu S \cdot sec^{n} \cdot cm^{-2}$ and ~4 $M\Omega \cdot cm^{2}$ and were not influenced

by the type of media. The small dependency of the oxide layer on the type of media was expected as such a layer is identical for the titanium electrodes in different wells. The R_S was calculated to be 53±6, 54±22, 34±2, 34±2, 32±2, and 6±4 $\Omega \cdot cm^2$ for DI water, HEPES, PBS, RPMI, DMEM, and Fe(II)Fe(III), respectively. The magnitude of R_S followed expectation of being decreased with the increase of ionic strength of the media. To better quantify any possible contribution of protein adsorption to the well impedance, the contribution of serum protein within RPMI media on the temporal impedance data was also evaluated. The results showed no significant difference in either R_S (R_M) or R_{CT} when compared to the other media.

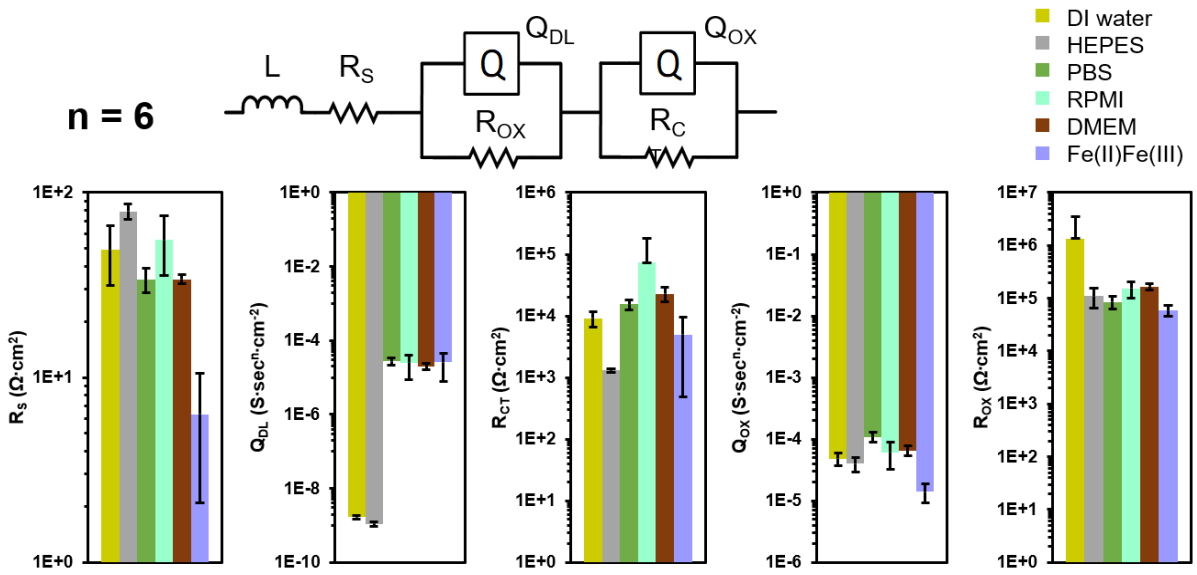

Figure 16. The results of equivalent circuit analysis of EIS data collected from six different media: DI water, 0.1 M HEPES, 0.01 M PBS, RPMI, DMEM, and Fe(II)Fe(III) at 37 °C.

4.4.3. Contribution of cell-culture insert to the impedance

The contribution of placing a microporous membrane (insert) to the impedance was evaluated in PBS and compared with the condition of having no insert. The results are reflected in **Table 8** and indicates that the presence of the insert (of any pore size) resulted in an increase of around 75% in

apparent solution (membrane) resistance, R_S, independent of the membrane pore size of the insert. The porous membrane allows the free transport of fluids between the compartments, however, as the results indicate, the presence of the insert affected the measured apparent solution resistance of the wells [143]. This is believed to arise from a membrane potential that opposes the streaming of ions through the membrane [144] [145].

Table 8. The effect of the presence of cell culture inserts with membrane pore size of 0.4 and 3 µm on the impedance of electroculture wells containing PBS (n=3).

	R_S ($\Omega \cdot cm^2$)
PBS (no insert)	46.4 ± 0.5
0.4 µm pore size	81.4 ± 5.3
3.0 µm pore size	79.4± 2.0

4.4.4. Simulation of electric field (EF) distribution within the well

The exploded version of the model used for analysis and response of the system to the application of 50 mV to the top and grounded bottom electrode of a single well are shown in **Figure 17**. A steadily decreasing field strength is observed along a line connecting the center of the two electrodes which peeks at the insert as the EF is stronger at the insulator based on Gauss's Law (**Figure 17D**). The EF on the membrane, **Figure 17E**, shown to be uniform across the membrane's surface confirms the uniformity assumption of EF in the design. The two far 0.5 mm region in the beginning and end of membrane are the edges where the membrane is sealed to the insert. The effect of insert porosity was also evaluated by assigning a weighted average permittivity (simple rule of mixtures) to the membrane based on the permittivity of PET ($\varepsilon = 3$) and PBS ($\varepsilon = 80$). **Figure 17E** show the 2D distribution of EF along a line connecting the center of top and bottom electrodes with increasing porosity from 0% (no membrane) to 100% (PET) in 10% increments

which shows the uniform EF distribution on the membrane. **Figure 17F** shows the EF and potential on top of the membrane as a function of porosity. As shown, the EF on top of membrane depends on the porosity and is highest when the porosity is 0% (pure PET) and decreases as the membrane become more porous. In practice, the porosity of commercially available membrane used in hanging cell culture insert is 10%-15%, therefore the cells do not experience a large difference in EF depending on the membrane porosity.

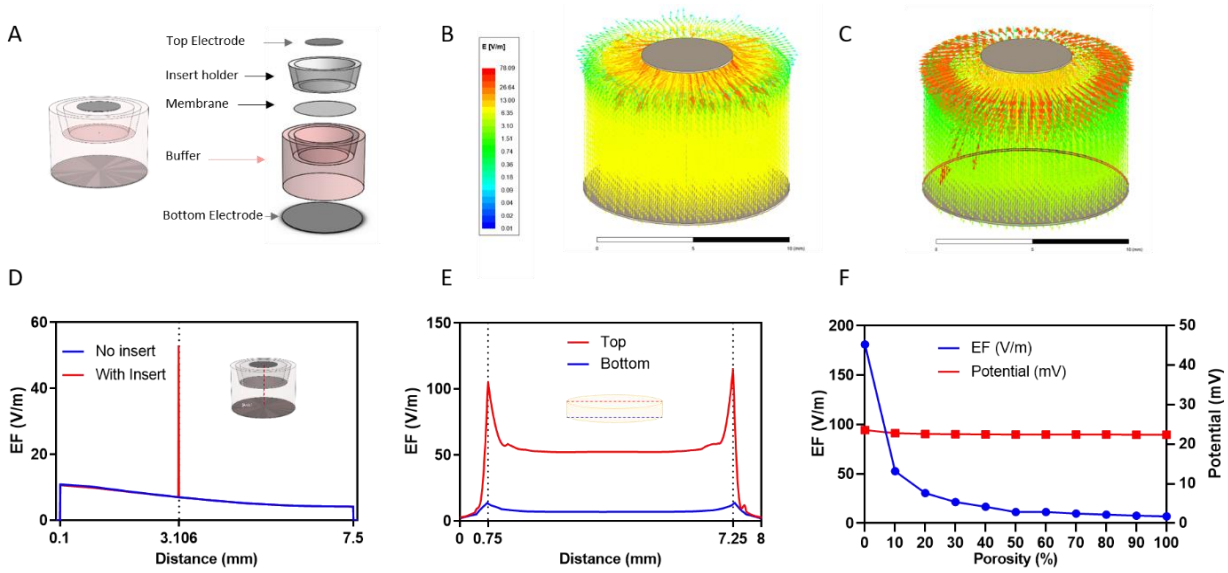

Figure 17. Electric field distribution within a single well of the 24-well electroculture plate: (A) An exploded view of the well model. The EF distribution between the two electrodes upon application of 50 mV with (B) no insert and (C) an insert of 10% membrane porosity. (D) The EF strength along a line connecting the top and bottom electrode when there is no insert and with insert of 10% porosity. (E) The EF strength along the diameter on the cell-bearing top and bottom surfaces. (F) The magnitude of EF (left) and potential (right) on the membrane (D= 3.106 mm) upon application of 50 mV as a function of membrane porosity (0 -100%).

4.4.5. EF effect on HUVECs monitored by EIS in ECSARA

According to the viability data presented in **Figure 18A**, during the first day, the HUVEC population of EF-stimulated group was smaller than control (0.8-fold), they outnumbered the control after 3 days (1.2 fold) and stayed at that level from day-4 onwards. The data suggest that

the growth was initially inhibited by EF stimulation but eventually adapted to support the proliferation of the cells until both test and control cells formed a confluent monolayer at about the fourth day of culture. Temporal changes in the extracted resistance of the cells (R_{cell}) measured over a five-day period are shown in **Figure 18C**. The R_{cell} was attributed to the combined presence of HUVECs on the porous membrane of the insert from the EQCRT corresponding to $LR_S(Q_{Cell}R_{Cell})(Q_{OX}R_{OX})(Q_{DL}R_{CT})$. The resistance of EF-stimulated and control cells started to increase at 54 h and 78 h, respectively and reached a constant level at 102 h. The resistance of the monolayer of HUVEC cells, known as TEER, has been vastly used as an indicator of formation of epithelial/endothelial monolayer and formation of tight junctions [146]. The growth rate of the HUVECs using viability data is shown in **Figure 18B** presents the ratio of the absorbance relative to the last time point (previous day) is in accordance with the EIS data where it is shown that EF-stimulated HUVECs reached to higher number/ confluency faster than control cells as have been reported previously [147, 148]. It is noteworthy that formation of tight junctions, clearly traceable with transmembrane resistance, could be different for different cell numbers since, while the cell population may increase, tight junctions may not form. The optical micrographs taken of sacrificed insert shows the approach to confluence as the HUVEC layer became established on the insert. The visualization of VE-cadherin, a protein expressed in tight junctions, confirmed that adjacent cells formed tight junctions, which resist ions/ molecules transport through the monolayer which reflected in the measured increase in resistance. The effect of EF on endothelial cells has been mostly investigated in terms of orientation and migration of these cells [149, 150], which in the case of the present study, as the plate is not designed to deliver the EF-parallel to the growth plane of the cells, no substantial changes in morphology was observed. The effectiveness of the EF on the expression of angiogenic factors by HUVECs *in-vitro* has been also reported [124, 151] which

shows the effect of FE beyond the morphometric parameters. The effect of shear stress and flow force in microfluidic system [152], inspired by the movement of blood in the vessels, have been vastly investigated and shown to clearly affect HUVECs [153]. EF as another type of force, could be compared to such mechanical stimulation. The positive effect of pulsatile signals on angiogenesis at frequencies similar to heart rate (72 beats/min corresponded to 1.2 Hz) [124, 154] could be supportive of the hypothesis of similarity between mechanical and electrical stimulations.

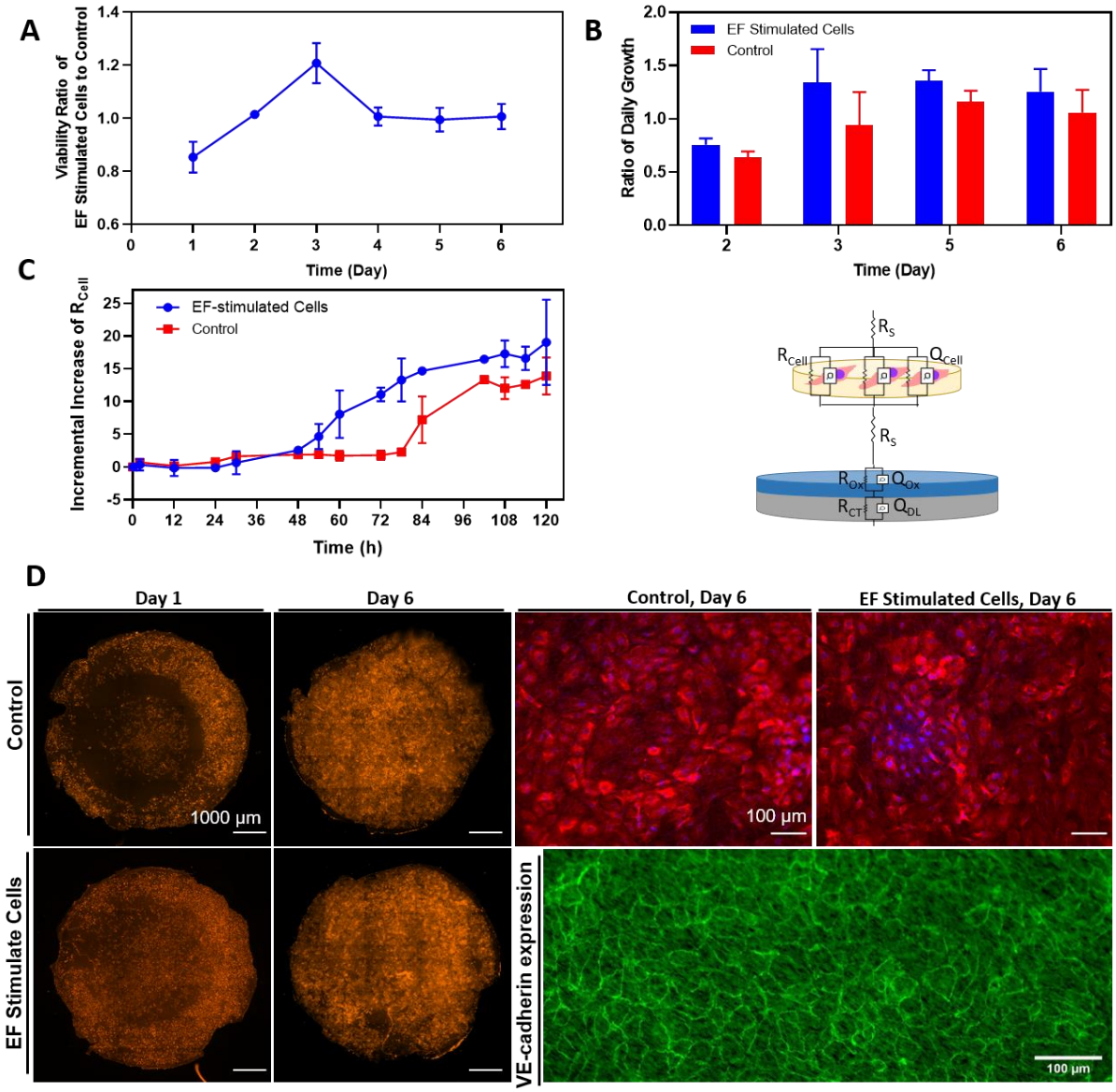

Figure 18. (A) Ratio of number of EF-stimulated to control cells and (B) ratio of daily population of cells compared to first day obtained from Alamar Blue assay. (C) The changes in the resistance (R_{Cell}) extracted from EIS data and schematic representation of the equivalent circuit elements used in the modeling of TEER. (D) The micrograph of sacrificed insert showing the HUVECs in EF stimulated and control stained for actin filaments and DAPI. Evidence of tight junction formation via fluorescent staining of HUVECs with anti VE-cadherin Alexa Flor® 488.

4.5. Conclusions

Electric field has been named as one of the influential factors in wide variety of phenomena from influencing chemical reactions to altering biological transport phenomena. An electrification system, the ECSARA, for the simultaneous EF stimulation and AC interrogation of cells has been designed, constructed, modeled and tested with HUVECs. The ECSARA offers a true bi-functional platform to study the influence of electrical stimulation and real-time monitoring of the response via EIS. Within the 24-well electroculture well format, a uniform electric field is applied to cells cultured on microporous membranes of cell culture inserts. Stable, reproducible measurement of impedance was demonstrated over a five-day cell culture period. A wide variety of media demonstrate stable performance with solution resistances that match the known ion concentrations and mobilities. ECSARA was used to apply electrical stimulation to HUVECs while monitoring the evolving impedance of the cells. The well-known *transepithelial*/transendothelial *electrical resistance* (*TEER*) was studied over a six-day day period and showed an increase of R_{Cell} as the cells grew to confluence in accordance with data collected from standard Alamar Blue viability assay. The EF showed to reduce the tie to confluency of HUVECs. Monitoring R_{Cell} confirmed the suitability of the ECSARA as a real-time monitoring device.

5. SUMMARY AND FUTURE WORK

Since Folkman and Haudenscild reported the occurrence of an in-vitro angiogenesis, [155], there is much advancement in tissue and regenerative engineering of cardiovascular-related biology. There is still much to learn and explore, after all human body evolved over millions of years. In this work the development of a hybrid hydrogel based on an inexpensive modification of gelatin was presented from the very early phase of development and characterization of the synthetic part, poly(HEMA-*co*-HPMA). The importance of water content and distribution, the main solvent of the hydrogel environment, was discussed and the hypothesis of crucial role of freezable: non-freezable bound water ratio on hydrogel's biotechnical properties was backed with experimental data and evidence. The control on the release of pre-loaded FITC-dextran from hydrogel by tuning the ratio of two main monomers, HEMA and HPMA from a burst-like to a gentler release profile was discussed. With the aim of rendering the polymer degradable, a straight-forward methacrylation modification of gelatin was used to synthesize GelMA which then photo-crosslinked along with other acryloyl-bearing monomers to yield a hybrid, degradable poly(GelMA-*co*-HEMA-*co*-HPMA) hydrogel. The mol% concentration of GelMA varied to tune the water content and distribution within the gel, compressive modulus, degradation rate, the release of pre-loaded growth factor surrogate FITC-dextran 40kDa, and cell attachment motifs. An inexpensive tunable platform was introduced and characterized which supports a wide range of application per requirements.

Aiming to apply electrical signals to the cells, a dual-function Electrical Cell Stimulation and Recording Apparatus was developed. The system developed to meet several needs and requirements, 1) the size and shape would be compatible with common cell culture practice setting which was addressed with a footprint of a common cell culture 24-well plate. This enabled the use

of standard trans-well cell culture insert for seeding the cells; 2) No direct seeding of cells on electrodes to avoid the transient changes in the media in vicinity of electrodes. This was met by using trans-well inserts which additionally provided a 3-D culture environment for the cells; 3) uniform electrical field along the cells growth plane, which addressed by embedding disk electrodes at top and bottom of each well which resulted in a uniform EF perpendicular to the plane where cells grow; 4) wide range of stimulation and minimal user involvement which was achieved via the use a function generator capable of delivering a wide range of waveforms, frequencies, and amplitudes. The whole system was controlled with a LabVIEW-developed interface towards automation. Additionally, the electrical stimulation mode, the system was designed to use powerful Electrical Impedance Spectroscopy (EIS) as a non-invasive tool for real-time monitoring of the cells. The characterization of the system confirmed a stable temporal response and non-significant well-to-well variation which are the prerequisite of a scientific experiment. The growth of endothelial cells in the system under mild electrical stimulation was studied and the suitability of using EIS monitoring tool was tested along with a standard viability assay. The results suggested an accelerated growth and faster onset of tight junction formation during a 5-day stimulation with pulses of 1.2 Hz frequency and 2 mS width delivering an electric field of 162 mV/mm strength.

The future work could include testing the paracrine release of VEGF from degradable poly(GelMA-*co*-HEMA-*co*-HPMA) hydrogels grown in either normal or electro-culture to study 1) the efficacy of controlled release of VEGF on growth of HUVECs, 2) the synergistic effect of VEGF and electro stimulation on cells. Additionally, to gain a fundamental insight into pathways through which the electric stimulation influences cells, analytical biological characterization such as RNA-seq, immunocytochemistry, and RT-PCR should be accompanied the studies.

REFERENCES

1. Vunjak-Novakovic, G. and David T. Scadden, Biomimetic Platforms for Human Stem Cell Research. Cell Stem Cell, 2011. **8**(3): p. 252-261.
2. Ma, P.X., Biomimetic materials for tissue engineering. Advanced Drug Delivery Reviews, 2008. **60**(2): p. 184-198.
3. Johari, B., et al., Repair of rat critical size calvarial defect using osteoblast-like and umbilical vein endothelial cells seeded in gelatin/hydroxyapatite scaffolds. Journal of Biomedical Materials Research Part A, 2016. **104**(7): p. 1770-1778.
4. Oswald, J., et al., Mesenchymal Stem Cells Can Be Differentiated Into Endothelial Cells In Vitro. STEM CELLS, 2004. **22**(3): p. 377-384.
5. Lozito, T.P., et al., Human mesenchymal stem cells express vascular cell phenotypes upon interaction with endothelial cell matrix. Journal of Cellular Biochemistry, 2009. **107**(4): p. 714-722.
6. Aizawa, Y., R. Wylie, and M. Shoichet, Endothelial Cell Guidance in 3D Patterned Scaffolds. Advanced Materials, 2010. **22**(43): p. 4831-4835.
7. Indentation Versus Tensile Measurements of Young's Modulus for Soft Biological Tissues. Tissue Engineering Part B: Reviews, 2011. **17**(3): p. 155-164.
8. Murikipudi, S., H. Methe, and E.R. Edelman, The effect of substrate modulus on the growth and function of matrix-embedded endothelial cells. Biomaterials, 2013. **34**(3): p. 677-684.
9. Clark, P., et al., Topographical control of cell behaviour: II. Multiple grooved substrata. Development, 1990. **108**(4): p. 635-644.

10. Janson, I.A. and A.J. Putnam, Extracellular matrix elasticity and topography: Material-based cues that affect cell function via conserved mechanisms. Journal of Biomedical Materials Research Part A, 2015. **103**(3): p. 1246-1258.
11. Grafting of Gelatin on Electrospun Poly(caprolactone) Nanofibers to Improve Endothelial Cell Spreading and Proliferation and to Control Cell Orientation. Tissue Engineering, 2005. **11**(7-8): p. 1149-1158.
12. Biodegradable Polymer Nanofiber Mesh to Maintain Functions of Endothelial Cells. Tissue Engineering, 2006. **12**(9): p. 2457-2466.
13. Abasi, S., J.R. Aggas, and A. Guiseppi-Elie, Physiochemical and morphological dependent growth of NIH/3T3 and PC-12 on polyaniline-chloride/chitosan bionanocomposites. Materials Science and Engineering: C, 2019. **99**: p. 1304-1312.
14. Abasi, S., et al., Design, fabrication and testing of an electrical cell stimulation and recording apparatus (ECSARA) for cells in electroculture. Biosensors and Bioelectronics, 2020. **147**: p. 111793.
15. Hosobuchi, Y., J. Adams, and R. Linchitz, Pain relief by electrical stimulation of the central gray matter in humans and its reversal by naloxone. Science, 1977. **197**(4299): p. 183-186.
16. García-Larrea, L., et al., Electrical stimulation of motor cortex for pain control: a combined PET-scan and electrophysiological study. PAIN, 1999. **83**(2): p. 259-273.
17. Vance, C.G.T., et al., Using TENS for pain control: the state of the evidence. Pain management, 2014. **4**(3): p. 197-209.
18. Kloth, L.C., Electrical Stimulation for Wound Healing: A Review of Evidence From In Vitro Studies, Animal Experiments, and Clinical Trials. The International Journal of Lower Extremity Wounds, 2005. **4**(1): p. 23-44.

19. Baker, L.L., et al., Effects of Electrical Stimulation on Wound Healing in Patients With Diabetic Ulcers. Diabetes Care, 1997. **20**(3): p. 405-412.

20. Al-Majed, A.A., et al., Brief Electrical Stimulation Promotes the Speed and Accuracy of Motor Axonal Regeneration. The Journal of Neuroscience, 2000. **20**(7): p. 2602-2608.

21. Geremia, N.M., et al., Electrical stimulation promotes sensory neuron regeneration and growth-associated gene expression. Experimental Neurology, 2007. **205**(2): p. 347-359.

22. Banerjee, P. and S. Ennis, Electrical muscle stimulation for heart failure: where do we stand? J. Clin. Exp. Cardiol., 2013. **4**: p. e120.

23. Guiseppi-Elie, A., Electroconductive hydrogels: Synthesis, characterization and biomedical applications. Biomaterials, 2010. **31**(10): p. 2701-2716.

24. Brown, D. and D. Usher, 1207. Hydrolysis of hydroxyalkyl phosphate esters: effect of changing ester group. Journal of the Chemical Society (Resumed), 1965: p. 6558-6564.

25. Zustiak, S.P. and J.B. Leach, Hydrolytically Degradable Poly(Ethylene Glycol) Hydrogel Scaffolds with Tunable Degradation and Mechanical Properties. Biomacromolecules, 2010. **11**(5): p. 1348-1357.

26. Gunatillake, P., R. Mayadunne, and R. Adhikari, Recent developments in biodegradable synthetic polymers, in Biotechnology Annual Review, M.R. El-Gewely, Editor. 2006, Elsevier. p. 301-347.

27. Doppalapudi, S., et al., Biodegradable polymers—an overview. Polymers for Advanced Technologies, 2014. **25**(5): p. 427-435.

28. Seliktar, D., et al., MMP-2 sensitive, VEGF-bearing bioactive hydrogels for promotion of vascular healing. Journal of Biomedical Materials Research Part A, 2004. **68A**(4): p. 704-716.

29. Salimath, A.S., et al., Dual delivery of hepatocyte and vascular endothelial growth factors via a protease-degradable hydrogel improves cardiac function in rats. PloS one, 2012. **7**(11): p. e50980-e50980.

30. Ottenbrite, R.M., K. Park, and T. Okano, eds. Biomedical Applications of Hydrogels Handbook. 1st Edition ed. 2010, Springer: New York. 700 p.

31. Buenger, D., F. Topuz, and J. Groll, Hydrogels in sensing applications. Progress in Polymer Science, 2012. **37**(12): p. 1678-1719.

32. Guenther, M. and G. Gerlach, Hydrogels for Chemical Sensors. Hydrogel Sensors and Actuators: Engineering and Technology, 2009. **6**: p. 165-195.

33. Brahim, S., D. Narinesingh, and A. Guiseppi-Elie, Polypyrrole-hydrogel composites for the construction of clinically important biosensors. Biosensors & Bioelectronics, 2002. **17**(1-2): p. 53-59.

34. Tavakoli, J. and Y. Tang, Hydrogel Based Sensors for Biomedical Applications: An Updated Review. Polymers, 2017. **9**(8): p. 364.

35. Jhon, M.S. and J.D. Andrade, Water and hydrogels. Journal of Biomedical Materials Research, 1973. **7**(6): p. 509-522.

36. Gun'ko, V., I. Savina, and S. Mikhalovsky, Properties of water bound in hydrogels. Gels, 2017. **3**(4): p. 37.

37. Lin, C.C. and A.T. Metters, Hydrogels in controlled release formulations: network design and mathematical modeling. Adv Drug Deliv Rev, 2006. **58**(12-13): p. 1379-408.

38. Guan, L., H. Xu, and D. Huang, The investigation on states of water in different hydrophilic polymers by DSC and FTIR. Journal of Polymer Research, 2011. **18**(4): p. 681-689.

39. Anseth, K.S., C.N. Bowman, and L. Brannon-Peppas, Mechanical properties of hydrogels and their experimental determination. Biomaterials, 1996. **17**(17): p. 1647-1657.

40. Ahmed, E.M., Hydrogel: Preparation, characterization, and applications: A review. Journal of advanced research, 2015. **6**(2): p. 105-121.

41. Nguyen, K.T. and J.L. West, Photopolymerizable hydrogels for tissue engineering applications. Biomaterials, 2002. **23**(22): p. 4307-4314.

42. Zhu, J.M. and R.E. Marchant, Design properties of hydrogel tissue-engineering scaffolds. Expert Review of Medical Devices, 2011. **8**(5): p. 607-626.

43. Alakpa, Enateri V., et al., Tunable Supramolecular Hydrogels for Selection of Lineage-Guiding Metabolites in Stem Cell Cultures. Chem, 2016. **1**(2): p. 298-319.

44. Bhat, A., J.M. Amanor-Boadu, and A. Guiseppi-Elie, Toward Impedimetric Measurement of Acidosis with a pH-Responsive Hydrogel Sensor. ACS Sensors, 2020.

45. Gun'ko, V.M., I.N. Savina, and S.V. Mikhalovsky, Properties of Water Bound in Hydrogels. Gels, 2017. **3**(4): p. 37.

46. Higuchi, A. and T. Iijima, D.S.C. investigation of the states of water in poly(vinyl alcohol-co-itaconic acid) membranes. Polymer, 1985. **26**(12): p. 1833-1837.

47. Ping, Z.H., et al., States of water in different hydrophilic polymers — DSC and FTIR studies. Polymer, 2001. **42**(20): p. 8461-8467.

48. Hatakeyama, T., K. Nakamura, and H. Hatakeyama, Determination of bound water content in polymers by DTA, DSC and TG. Thermochimica Acta, 1988. **123**: p. 153-161.

49. Hodge, R.M., G.H. Edward, and G.P. Simon, Water absorption and states of water in semicrystalline poly(vinyl alcohol) films. Polymer, 1996. **37**(8): p. 1371-1376.

50. Tamai, Y., H. Tanaka, and K. Nakanishi, Molecular Dynamics Study of Polymer−Water Interaction in Hydrogels. 2. Hydrogen-Bond Dynamics. Macromolecules, 1996. **29**(21): p. 6761-6769.

51. Müller-Plathe, F., Different States of Water in Hydrogels? Macromolecules, 1998. **31**(19): p. 6721-6723.

52. Burghoff, H.-G. and W. Pusch, Characterization of water structure in cellulose acetate membranes by calorimetric measurements. Journal of Applied Polymer Science, 1979. **23**(2): p. 473-484.

53. Finosh, G.T., et al., Hybrid alginate-polyester bimodal network hydrogel for tissue engineering – Influence of structured water on long-term cellular growth. Colloids and Surfaces B: Biointerfaces, 2015. **135**: p. 855-864.

54. Andrade, J.D., et al., WATER AS A BIOMATERIAL. ASAIO Journal, 1973. **19**(1): p. 1-7.

55. Guiseppi-Elie, A., C. Dong, and C.Z. Dinu, Crosslink density of a biomimetic poly(HEMA)-based hydrogel influences growth and proliferation of attachment dependent RMS 13 cells. Journal of Materials Chemistry, 2012. **22**(37): p. 19529-19539.

56. Abraham, S., et al., Molecularly engineered p(HEMA)-based hydrogels for implant biochip biocompatibility. Biomaterials, 2005. **26**(23): p. 4767-4778.

57. Brahim, S., D. Narinesingh, and A. Guiseppi-Elie, Synthesis and Hydration Properties of pH-Sensitive p(HEMA)-Based Hydrogels Containing 3-(Trimethoxysilyl)propyl Methacrylate. Biomacromolecules, 2003. **4**(3): p. 497-503.

58. Kotanen, C.N., et al., The effect of the physicochemical properties of bioactive electroconductive hydrogels on the growth and proliferation of attachment dependent cells. Biomaterials, 2013. **34**(27): p. 6318-6327.

59. Bouwstra, J.A., M.A. Salomons-de Vries, and J.C. van Miltenburg, The thermal behaviour of water in hydrogels. Thermochimica Acta, 1995. **248**: p. 319-327.

60. Brahim, S., D. Narinesingh, and A. Guiseppi-Elie, Release characteristics of novel pH-sensitive p (HEMA-DMAEMA) hydrogels containing 3-(trimethoxy-silyl) propyl methacrylate. Biomacromolecules, 2003. **4**(5): p. 1224-1231.

61. Xu, X.D., et al., "Click" chemistry forin situformation of thermoresponsive P(NIPAAm-co-HEMA)-based hydrogels. Journal of Polymer Science Part A: Polymer Chemistry, 2008. **46**(15): p. 5263-5277.

62. Yang, X., et al., Multi-stimuli-responsive poly (NIPA-co-HEMA-co-NVP) with spironaphthoxazine hydrogel for optical data storage application. 2016. **294**(10): p. 1623-1632.

63. Brahim, S., D. Narinesingh, and A. Guiseppi-Elie, Polypyrrole-hydrogel composites for the construction of clinically important biosensors. Biosensors and Bioelectronics, 2002. **17**(1-2): p. 53-59.

64. Aucoin, H., et al., Release of Potassium Ion and Calcium Ion from Phosphorylcholine Group Bearing Hydrogels. Polymers, 2013. **5**(4): p. 1241.

65. Kopeček, J. and P. Kopečková, HPMA copolymers: origins, early developments, present, and future. Advanced drug delivery reviews, 2010. **62**(2): p. 122-149.

66. Plant, G.W., S. Woerly, and A.R. Harvey, Hydrogels containing peptide or aminosugar sequences implanted into the rat brain: influence on cellular migration and axonal growth. Experimental neurology, 1997. **143**(2): p. 287-299.

67. Kopeček, J. and H. Bažilová, Poly [N-(2-hydroxypropyl) methacrylamide]—I. Radical polymerization and copolymerization. European Polymer Journal, 1973. **9**(1): p. 7-14.

68. Yang, J. and J. Kopeček, Macromolecular therapeutics. Journal of Controlled Release, 2014. **190**: p. 288-303.

69. Kola ik, J., et al., Relaxation Behavior of Poly (N-monosubstituted Methacrylamides). International Journal of Polymeric Materials, 1976. **5**(1-2): p. 89-97.

70. Chytil, P., et al., Synthesis and Properties of Star HPMA Copolymer Nanocarriers Synthesised by RAFT Polymerisation Designed for Selective Anticancer Drug Delivery and Imaging. Macromolecular Bioscience, 2015. **15**(6): p. 839-850.

71. Ulbrich, K., et al., Targeted Drug Delivery with Polymers and Magnetic Nanoparticles: Covalent and Noncovalent Approaches, Release Control, and Clinical Studies. Chemical Reviews, 2016. **116**(9): p. 5338-5431.

72. Resmi, R., et al., Synthesis and characterization of silver nanoparticle incorporated gelatin-hydroxypropyl methacrylate hydrogels for wound dressing applications. Journal of Applied Polymer Science, 2017. **134**(10).

73. Flory, P.J., Principles of polymer chemistry. 1953.

74. La Scala, J. and R.P. Wool, Property analysis of triglyceride-based thermosets. Polymer, 2005. **46**(1): p. 61-69.

75. Lee, K.Y., et al., Controlling Mechanical and Swelling Properties of Alginate Hydrogels Independently by Cross-Linker Type and Cross-Linking Density. Macromolecules, 2000. **33**(11): p. 4291-4294.

76. Aggas, J.R., et al., Microfabricated and 3-D Printed Soft Bioelectronic Constructs from PAn-PAAMPSA-Containing Hydrogels. Bioengineering, 2018. **5**(4): p. 87.

77. Abasi, S., et al., Biotechnical Properties of Poly(HEMA-co-HPMA) Hydrogels Are Governed by Distribution among Water States. ACS Biomaterials Science & Engineering, 2019. **5**(10): p. 4994-5004.

78. Abasi, S., et al., Distribution of water states within Poly(HEMA-co-HPMA)-based hydrogels. Polymer, 2019. **185**: p. 121978.

79. Boztas, A.O. and A. Guiseppi-Elie, Immobilization and Release of the Redox Mediator Ferrocene Monocarboxylic Acid from within Cross-Linked p(HEMA-co-PEGMA-co-HMMA) Hydrogels. Biomacromolecules, 2009. **10**(8): p. 2135-2143.

80. Van Krevelen, D.W. and K. Te Nijenhuis, Properties of polymers: their correlation with chemical structure; their numerical estimation and prediction from additive group contributions. 2009: Elsevier.

81. Miložič, N., et al., Evaluation of diffusion coefficient determination using a microfluidic device. 2014. **28**(2): p. 215-223.

82. Kotanen, C.N., et al., Partitioning of coomassie brilliant blue into DMAEMA containing poly (HEMA)-based hydrogels. European Polymer Journal, 2015. **72**: p. 438-450.

83. Bhat, A., et al., Molecular engineering of poly(HEMA-co-PEGMA)-based hydrogels: Role of minor AEMA and DMAEMA inclusion. Materials Science and Engineering: C, 2019. **98**: p. 89-100.

84. Chinga, G., et al., Quantification of the 3D microstructure of SC surfaces. J Microsc, 2007. **227**(Pt 3): p. 254-65.

85. Ritger, P.L. and N.A. Peppas, A simple equation for description of solute release II. Fickian and anomalous release from swellable devices. Journal of controlled release, 1987. **5**(1): p. 37-42.

86. Ganji, F., F.S. VASHEGHANI, and F.E. VASHEGHANI, Theoretical description of hydrogel swelling: a review. 2010.

87. Ritger, P.L. and N.A. Peppas, A simple equation for description of solute release I. Fickian and non-fickian release from non-swellable devices in the form of slabs, spheres, cylinders or discs. Journal of Controlled Release, 1987. **5**(1): p. 23-36.

88. Ganji, F., S. Vasheghani-Farahani, and E. Vasheghani-Farahani, Theoretical Description of Hydrogel Swelling: A Review. Iranian Polymer Journal, 2010. **19**(5): p. 375-398.

89. Serra, L., J. Doménech, and N.A. Peppas, Drug transport mechanisms and release kinetics from molecularly designed poly(acrylic acid-g-ethylene glycol) hydrogels. Biomaterials, 2006. **27**(31): p. 5440-5451.

90. Impedance spectroscopy. Annu. Biomed. Eng., 1992. **20**(3): p. 289.

91. Serra, L., J. Doménech, and N.A. Peppas, Drug transport mechanisms and release kinetics from molecularly designed poly (acrylic acid-g-ethylene glycol) hydrogels. Biomaterials, 2006. **27**(31): p. 5440-5451.

92. Nam, C., et al., Increased Hydrogel Swelling Induced by Absorption of Small Molecules. ACS Applied Materials & Interfaces, 2016. **8**(22): p. 14263-14270.

93. Freedman, H.H.J.J.o.t.A.C.S., Intramolecular H-bonds. I. A spectroscopic study of the hydrogen bond between hydroxyl and nitrogen. Journal of the American Chemical Society, 1961. **83**(13): p. 2900-2905.

94. Sekine, Y., et al., Dependence of structure of polymer side chain on water structure in hydrogels. Polymer, 2014. **55**(24): p. 6320-6324.

95. Giauque, W.F. and J.W. Stout, The Entropy of Water and the Third Law of Thermodynamics. The Heat Capacity of Ice from 15 to 273°K. Journal of the American Chemical Society, 1936. **58**(7): p. 1144-1150.

96. Angell, C.A. and J.C. Tucker, Anomalous Heat Capacities of Supercooled Water and Heavy Water. Science, 1973. **181**(4097): p. 342-344.

97. Sippola, H. and P. Taskinen, Activity of Supercooled Water on the Ice Curve and Other Thermodynamic Properties of Liquid Water up to the Boiling Point at Standard Pressure. Journal of Chemical & Engineering Data, 2018. **63**(8): p. 2986-2998.

98. Higuchi, A. and T. Iijima, D.s.c. investigation of the states of water in poly(vinyl alcohol) membranes. Polymer, 1985. **26**(8): p. 1207-1211.

99. Greenberg, A. and R. Kusy, Influence of crosslinking on the glass transition of poly (acrylic acid). Journal of Applied Polymer Science, 1980. **25**(8): p. 1785-1788.

100. Guiseppi-Elie, A., C. Dong, and C.Z. Dinu, Crosslink density of a biomimetic poly (HEMA)-based hydrogel influences growth and proliferation of attachment dependent RMS 13 cells. Journal of Materials Chemistry, 2012. **22**(37): p. 19529-19539.

101. Nielsen, L.E., Cross-Linking–Effect on Physical Properties of Polymers. Journal of Macromolecular Science, Part C, 1969. **3**(1): p. 69-103.

102. Bajpai, A.K., et al., Responsive polymers in controlled drug delivery. Progress in Polymer Science, 2008. **33**(11): p. 1088-1118.

103. Tamai, Y., H. Tanaka, and K. Nakanishi, Molecular Dynamics Study of Water in Hydrogels. Molecular Simulation, 1996. **16**(4-6): p. 359-374.

104. Hoare, T.R. and D.S. Kohane, Hydrogels in drug delivery: Progress and challenges. Polymer, 2008. **49**(8): p. 1993-2007.

105. Huang, X. and C.S. Brazel, On the importance and mechanisms of burst release in matrix-controlled drug delivery systems. J Control Release, 2001. **73**(2-3): p. 121-36.

106. Koetting, M.C., et al., Stimulus-responsive hydrogels: Theory, modern advances, and applications. Materials Science and Engineering: R: Reports, 2015. **93**: p. 1-49.

107. Bhat, A., et al., Dataset on hydrophobicity indices and differential scanning calorimetry thermograms for poly(HEMA)-based hydrogels. Data in Brief, 2019. **24**: p. 103891.

108. Guo, Q., P.T. Knight, and P.T. Mather, Tailored drug release from biodegradable stent coatings based on hybrid polyurethanes. Journal of Controlled Release, 2009. **137**(3): p. 224-233.

109. Peppas, N.A. and R.W. Korsmeyer, Dynamically swelling hydrogels in controlled release applications. Hydrogels in medicine and pharmacy, 1987. **3**: p. 109-136.

110. Thomas, N.L. and A.H. Windle, A theory of case II diffusion. Polymer, 1982. **23**(4): p. 529-542.

111. Yamada, M., et al., Electrical Stimulation Modulates Fate Determination of Differentiating Embryonic Stem Cells. STEM CELLS, 2007. **25**(3): p. 562-570.

112. Robinson, K.R., The responses of cells to electrical fields: a review. The Journal of Cell Biology, 1985. **101**(6): p. 2023-2027.

113. Famm, K., et al., A jump-start for electroceuticals. Nature, 2013. **496**: p. 159.

114. Huang, C.Q., P.M. Carter, and R.K. Shepherd, Stimulus Induced pH Changes in Cochlear Implants: An In Vitro and In Vivo Study. Annals of Biomedical Engineering, 2001. **29**(9): p. 791-802.

115. Brummer, S.B. and M.J. Turner, Electrochemical Considerations for Safe Electrical Stimulation of the Nervous System with Platinum Electrodes. IEEE Transactions on Biomedical Engineering, 1977. **BME-24**(1): p. 59-63.

116. Song, B., et al., Application of direct current electric fields to cells and tissues in vitro and modulation of wound electric field in vivo. Nature Protocols, 2007. **2**: p. 1479.

117. Tandon, N., et al. Design of electrical stimulation bioreactors for cardiac tissue engineering. in 2008 30th Annual International Conference of the IEEE Engineering in Medicine and Biology Society. 2008.

118. Xiong, G.M., et al., Development of a miniaturized stimulation device for electrical stimulation of cells. Journal of Biological Engineering, 2015. **9**(1): p. 14.

119. Mobini, S., L. Leppik, and J.H. Barker, Direct current electrical stimulation chamber for treating cells in vitro. BioTechniques, 2016. **60**(2): p. 95-98.

120. Ping, J., et al., Adhesive curing through low-voltage activation. Nature Communications, 2015. **6**: p. 8050.

121. Gan, L., et al., Self curing and voltage activated catechol adhesives. Chemical Communications, 2019.

122. Poo, M.-m. and K.R. Robinson, Electrophoresis of concanavalin A receptors along embryonic muscle cell membrane. Nature, 1977. **265**(5595): p. 602-605.

123. Tandon, N., et al. Characterization of Electrical Stimulation Electrodes for Cardiac Tissue Engineering. in 2006 International Conference of the IEEE Engineering in Medicine and Biology Society. 2006.

124. Yuan, X., et al., Electrical stimulation enhances cell migration and integrative repair in the meniscus. Scientific Reports, 2014. **4**: p. 3674.

125. Bieberich, E. and A. Guiseppi-Elie, Neuronal differentiation and synapse formation of PC12 and embryonic stem cells on interdigitated microelectrode arrays:: Contact structures for neuron-to-electrode signal transmission (NEST). Biosensors and Bioelectronics, 2004. **19**(8): p. 923-931.

126. Griffin, M. and A. Bayat, Electrical stimulation in bone healing: critical analysis by evaluating levels of evidence. Eplasty, 2011. **11**: p. e34-e34.

127. Fujita, H., T. Nedachi, and M. Kanzaki, Accelerated de novo sarcomere assembly by electric pulse stimulation in C2C12 myotubes. Experimental Cell Research, 2007. **313**(9): p. 1853-1865.

128. Giaever, I. and C.R. Keese, Monitoring fibroblast behavior in tissue culture with an applied electric field. Proceedings of the National Academy of Sciences, 1984. **81**(12): p. 3761-3764.

129. Williams, J.C., et al., Complex impedance spectroscopy for monitoring tissue responses to inserted neural implants. Journal of Neural Engineering, 2007. **4**(4): p. 410-423.

130. Zhang, Y.S., et al., Multisensor-integrated organs-on-chips platform for automated and continual in situ monitoring of organoid behaviors. Proceedings of the National Academy of Sciences, 2017. **114**(12): p. E2293-E2302.

131. Adcock, A.F., C.O. Agbai, and L. Yang, Application of electric cell-substrate impedance sensing toward personalized anti-cancer therapeutic selection. Journal of Analytical Science and Technology, 2018. **9**(1): p. 17.

132. Justin, G., et al., Biomimetic hydrogels for biosensor implant biocompatibility: electrochemical characterization using micro-disc electrode arrays (MDEAs). Biomedical Microdevices, 2009. **11**(1): p. 103-115.

133. Lo, C.M., C.R. Keese, and I. Giaever, Impedance analysis of MDCK cells measured by electric cell-substrate impedance sensing. Biophysical Journal, 1995. **69**(6): p. 2800-2807.

134. Lo, C.-M. and J. Ferrier, Impedance analysis of fibroblastic cell layers measured by electric cell-substrate impedance sensing. Physical Review E, 1998. **57**(6): p. 6982-6987.

135. Xing, J.Z., et al., Dynamic Monitoring of Cytotoxicity on Microelectronic Sensors. Chemical Research in Toxicology, 2005. **18**(2): p. 154-161.

136. Wegener, J., et al., Automated multi-well device to measure transepithelial electrical resistances under physiological conditions. BioTechniques, 2004. **37**(4): p. 590-597.

137. Franks, W., et al., Impedance characterization and modeling of electrodes for biomedical applications. IEEE Transactions on Biomedical Engineering, 2005. **52**(7): p. 1295-1302.

138. Suni, I.I., Impedance methods for electrochemical sensors using nanomaterials. TrAC Trends in Analytical Chemistry, 2008. **27**(7): p. 604-611.

139. Yang, L. and A. Guiseppi-Elie, Impedimetric Biosensors for Nano- and Microfluidics, in Encyclopedia of Microfluidics and Nanofluidics, D. Li, Editor. 2008, Springer US: Boston, MA. p. 811-823.

140. Dellis, J.-L., ZFit, in MATLAB. 2010, MathWorks, Natick, MA: MathWorks.

141. Tamilselvi, S., R. Vedarajan, and R. Nallaiyan, Corrosion behaviour of Ti–6Al–7Nb and Ti–6Al–4V ELI alloys in the simulated body fluid solution by electrochemical impedance spectroscopy. Vol. 52. 2006. 839-846.

142. Brown, M.A., A. Goel, and Z. Abbas, Effect of Electrolyte Concentration on the Stern Layer Thickness at a Charged Interface. Angewandte Chemie International Edition, 2016. **55**(11): p. 3790-3794.

143. Huang, Q., et al., The effect of electrolyte concentration on electrochemical impedance for evaluating polysulfone membranes. Environmental Science: Water Research & Technology, 2018. **4**(8): p. 1145-1151.

144. Kasianowicz, J.J., et al., Characterization of individual polynucleotide molecules using a membrane channel. Proceedings of the National Academy of Sciences, 1996. **93**(24): p. 13770-13773.

145. Ho, C., et al., Electrolytic transport through a synthetic nanometer-diameter pore. Proceedings of the National Academy of Sciences of the United States of America, 2005. **102**(30): p. 10445-10450.

146. Benson, K., S. Cramer, and H.-J. Galla, Impedance-based cell monitoring: barrier properties and beyond. Fluids and Barriers of the CNS, 2013. **10**(1): p. 5.

147. Li, Y., et al., Enhanced adhesion and proliferation of human umbilical vein endothelial cells on conductive PANI-PCL fiber scaffold by electrical stimulation. Materials Science and Engineering: C, 2017. **72**: p. 106-112.

148. Yen-Patton, G.P.A., et al., Endothelial cell response to pulsed electromagnetic fields: Stimulation of growth rate and angiogenesis in vitro. Journal of Cellular Physiology, 1988. **134**(1): p. 37-46.

149. Zhao, M., et al., Electrical stimulation directly induces pre-angiogenic responses in vascular endothelial cells by signaling through VEGF receptors. Journal of Cell Science, 2004. **117**(3): p. 397-405.

150. Li, X. and J. Kolega, Effects of Direct Current Electric Fields on Cell Migration and Actin Filament Distribution in Bovine Vascular Endothelial Cells. Journal of Vascular Research, 2002. **39**(5): p. 391-404.

151. Geng, K., et al., Electrical stimulation facilitates the angiogenesis of human umbilical vein endothelial cells through MAPK/ERK signaling pathway by stimulating FGF2 secretion. American Journal of Physiology-Cell Physiology, 2019. **317**(2): p. C277-C286.

152. Mathur, T., et al., Organ-on-chips made of blood: endothelial progenitor cells from blood reconstitute vascular thromboinflammation in vessel-chips. Lab on a Chip, 2019. **19**(15): p. 2500-2511.

153. Song, J.W. and L.L. Munn, Fluid forces control endothelial sprouting. Proceedings of the National Academy of Sciences, 2011. **108**(37): p. 15342-15347.

154. Au, H.T.H., et al., Interactive effects of surface topography and pulsatile electrical field stimulation on orientation and elongation of fibroblasts and cardiomyocytes. Biomaterials, 2007. **28**(29): p. 4277-4293.

155. Folkman, J. and C. Haudenschild, Angiogenesis in vitro. Nature, 1980. **288**(5791): p. 551-556.